Astronomy & Astrophysics

GRAVITY chromatic imaging of η Car's core

Milliarcsecond resolution imaging of the wind-wind collision zone (Brγ, He ɪ)

GRAVITY Collaboration[*]: J. Sanchez-Bermudez[1,8], G. Weigelt[11], J. M. Bestenlehner[1,15], P. Kervella[2,13],
W. Brandner[1], Th. Henning[1], A. Müller[1], G. Perrin[2], J.-U. Pott[1], M. Schöller[7], R. van Boekel[1], R. Abuter[7],
M. Accardo[7], A. Amorim[6,19], N. Anugu[6,20], G. Ávila[7], M. Benisty[3,13], J. P. Berger[3,7], N. Blind[16], H. Bonnet[7],
P. Bourget[8], R. Brast[7], A. Buron[9], F. Cantalloube[1], A. Caratti o Garatti[1,10], F. Cassaing[17], F. Chapron[2], E. Choquet[2],
Y. Clénet[2], C. Collin[2], V. Coudé du Foresto[2], W. de Wit[8], T. de Zeeuw[7,14], C. Deen[9], F. Delplancke-Ströbele[7],
R. Dembet[7], F. Derie[7], J. Dexter[9], G. Duvert[3], M. Ebert[1], A. Eckart[4,11], F. Eisenhauer[9], M. Esselborn[7], P. Fédou[2],
P. J. V. Garcia[5,6], C. E. Garcia Dabo[7], R. Garcia Lopez[1,10], F. Gao[9], E. Gendron[2], R. Genzel[9,12], S. Gillessen[9],
X. Haubois[8], M. Haug[7,9], F. Haussmann[9], S. Hippler[1], M. Horrobin[4], A. Huber[1], Z. Hubert[1,2], N. Hubin[7],
C. A. Hummel[7], G. Jakob[7], L. Jochum[7], L. Jocou[3], M. Karl[9], A. Kaufer[8], S Kellner[9,11], S. Kendrew[1,18], L. Kern[7],
M. Kiekebusch[7], R. Klein[1], J. Kolb[8], M. Kulas[1], S. Lacour[2], V. Lapeyrère[2], B. Lazareff[3], J.-B. Le Bouquin[3], P. Léna[2],
R. Lenzen[1], S. Lévêque[7], M. Lippa[9], Y. Magnard[3], L. Mehrgan[7], M. Mellein[1], A. Mérand[7], J. Moreno-Ventas[1],
T. Moulin[3], E. Müller[1,7], F. Müller[1], U. Neumann[3], S. Oberti[7], T. Ott[9], L. Pallanca[8], J. Panduro[1], L. Pasquini[7],
T. Paumard[2], I. Percheron[7], K. Perraut[3], P.-O. Petrucci[3], A. Pflüger[9], O. Pfuhl[9], T. P. Duc[7], P. M. Plewa[9], D. Popovic[7],
S. Rabien[9], A. Ramirez[8], J. Ramos[1], C. Rau[9], M. Riquelme[8], G. Rodríguez-Coira[2], R.-R. Rohloff[1], A. Rosales[9],
G. Rousset[2], S. Scheithauer[1], N. Schuhler[8], J Spyromilio[7], O. Straub[2], C. Straubmeier[4], E. Sturm[9], M Suarez[7],
K. R. W. Tristram[8], N. Ventura[3], F. Vincent[2], I. Waisberg[9], I. Wank[4], F. Widmann[9], E. Wieprecht[9], M. Wiest[4],
E. Wiezorrek[9], M. Wittkowski[7], J. Woillez[7], B. Wolff[7], S. Yazici[4,9], D. Ziegler[2], and G. Zins[8]

(Affiliations can be found after the references)

ABSTRACT

Context. η Car is one of the most intriguing luminous blue variables in the Galaxy. Observations and models of the X-ray, ultraviolet, optical, and infrared emission suggest a central binary in a highly eccentric orbit with a 5.54 yr period residing in its core. 2D and 3D radiative transfer and hydrodynamic simulations predict a primary with a dense and slow stellar wind that interacts with the faster and lower density wind of the secondary. The wind-wind collision scenario suggests that the secondary's wind penetrates the primary's wind creating a low-density cavity in it, with dense walls where the two winds interact. However, the morphology of the cavity and its physical properties are not yet fully constrained.
Aims. We aim to trace the inner ∼5–50 au structure of η Car's wind-wind interaction, as seen through Brγ and, for the first time, through the He ɪ 2s-2p line.
Methods. We have used spectro-interferometric observations with the *K*-band beam-combiner GRAVITY at the VLTI. The analyses of the data include (i) parametrical model-fitting to the interferometric observables, (ii) a CMFGEN model of the source's spectrum, and (iii) interferometric image reconstruction.
Results. Our geometrical modeling of the continuum data allows us to estimate its FWHM angular size close to 2 mas and an elongation ratio $\epsilon = 1.06 \pm 0.05$ over a PA = $130° \pm 20°$. Our CMFGEN modeling of the spectrum helped us to confirm that the role of the secondary should be taken into account to properly reproduce the observed Brγ and He ɪ lines. Chromatic images across the Brγ line reveal a southeast arc-like feature, possibly associated to the hot post-shocked winds flowing along the cavity wall. The images of the He ɪ 2s-2p line served to constrain the 20 mas (∼50 au) structure of the line-emitting region. The observed morphology of He ɪ suggests that the secondary is responsible for the ionized material that produces the line profile. Both the Brγ and the He ɪ 2s-2p maps are consistent with previous hydrodynamical models of the colliding wind scenario. Future dedicated simulations together with an extensive interferometric campaign are necessary to refine our constraints on the wind and stellar parameters of the binary, which finally will help us predict the evolutionary path of η Car.

Key words. instrumentation: interferometers – instrumentation: high angular resolution – stars: mass-loss – stars: massive – stars: imaging – binaries: general

1. Introduction

Massive stars are among the most important chemical factories of the interstellar medium (ISM). This is mainly because their evolution and fate are highly affected by strong stellar winds ($v_{\rm w} \sim 10^3$ km s^{-1}), high mass-loss rates ($\dot{M} \sim 10^{-5}$–10^{-3} $M_\odot$ yr^{-1}) and deaths as supernovae (SNe; see, e.g., Conti & Niemelä 1976; Langer et al. 1994; Meynet & Maeder 2003; Meynet et al. 2011).
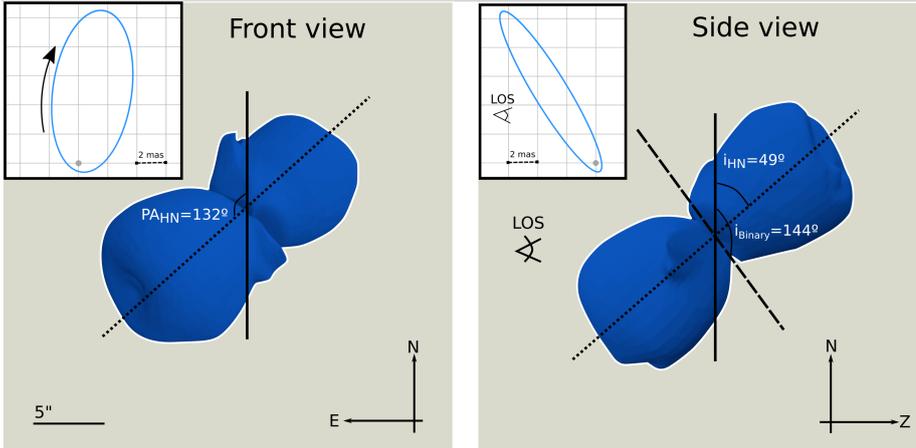
One of the evolutionary stages of high-mass stars that exhibit sporadic but violent mass-loss episodes is the luminous blue variable (LBV) phase (Humphreys & Davidson 1994). The importance of LBVs to stellar evolution models relies on the possibility of them to directly explode as SN without being a Wolf-Rayet (WR) star (Smith 2007; Smith et al. 2011; Trundle et al. 2008). Therefore, detailed studies of LBVs are crucial to understand the mass-loss processes in high-mass stars (see e.g., Pastorello et al. 2010; Smith et al. 2011).

The source, η Car, is one of the most intriguing LBVs in the Galaxy. Located at the core of the Homunculus Nebula in the Trumpler 16 cluster at a distance of 2.3 ± 0.1 kpc (Walborn 1973; Allen & Hillier 1993; Smith 2006), it has been identified as a luminous ($L_{tot} \geq 5 \times 10^6 L_\odot$ Davidson & Humphreys 1997; Smith et al. 2003) colliding-wind binary (Damineli et al. 1997, 2008a,b; Hillier et al. 2001; Corcoran et al. 2010) in a highly eccentric orbit ($e \sim 0.9$; Corcoran 2005) with a period of 2022.7 ± 1.3 d (Damineli et al. 2008a).

The primary, η_A, is a very massive star with an estimated $M \sim 100\ M_\odot$, a mass-loss rate $\dot{M} \sim 8.5 \times 10^{-4}\ M_\odot\ yr^{-1}$ and a wind terminal speed $v_\infty \sim 420\ km\,s^{-1}$ (Hillier et al. 2001, 2006; Groh et al. 2012a,b). Evidence suggests that η_A is near the Eddington limit (Conti 1984; Humphreys & Davidson 1994). Therefore, it loses substantial mass in violent episodes such as the "Great Eruption" where ~15 $M_\odot$, possibly more than 40 $M_\odot$ (Gomez et al. 2010; Morris et al. 2017), were ejected over a period of ~10 yr. Mass-loss events dominate the evolutionary tracks of the most massive stars (Langer 1998; Smith 2006). In binary star systems, like η Car, the presence of a companion affects wind-driven mass loss, providing alternative evolutionary pathways compared to single stars. Therefore, understanding in detail their mass-loss processes is particularly important.

The nature of the secondary, η_B, is even less constrained since it has not been directly observed (it is, at least, of the order of 100 times fainter than η_A; Weigelt et al. 2007) because it is embedded in the dense wind of the primary. Models of the X-ray emission ($kT \sim 4-5\ keV$) predict a wind terminal velocity $v_\infty \sim 3000\ km\,s^{-1}$, a mass-loss rate $\dot{M} \sim 10^{-5}\ M_\odot\ yr^{-1}$ (Pittard & Corcoran 2002; Okazaki et al. 2008; Parkin et al. 2011), and a $T_{eff} \sim 36\,000-41\,000\ K$ (Teodoro et al. 2008).

Models of the mutual motion of the stars suggest an inclination $i \sim 130-145°$, an argument of periastron $\omega \sim 240-285°$, and a sky projected PA $\sim 302-327°$ for the best-fit orbital solution (Damineli et al. 1997; Okazaki et al. 2008; Parkin et al.

2009, 2011; Groh et al. 2010b; Gull et al. 2011; Madura & Groh 2012; Madura et al. 2012; Teodoro et al. 2016). This suggests that the orbital plane of the binary is almost perpendicular to the Homunculus axis ($i \sim 49°$ with respect to the sky plane; PA $\sim 132°$; Davidson et al. 2001; Smith 2006). These orbital parameters also imply that the secondary remains in front of the primary (in the line-of-sight -LOS- of the observer) most of the time during the orbital motion, except close to the periastron, where η_B goes behind η_A and it is obscured by the dense primary wind.

Figure 1 displays the inclination and PA of the Homunculus Nebula and of the orbit of η_B around η_A, according to the orbital solution reported by Teodoro et al. (2016). The left panel displays the nebula projected in the plane of the sky. The PA (east to the north) of the semi-major axis is labeled in the image. The right panel displays the position of the nebula and of the orbit of the binary in a plane parallel to the observer's line-of-sight and the sky plane. The inclination angles (relative to the sky plane) of the nebula (i_{HN}) and of the binary's orbital plane (i_{Binary}) are labeled.

The secondary, η_B, photoionizes part of the primary wind, changing the strength of lines such as Hα, He I, [Fe II], and [Ne II] (Hillier et al. 2001; Nielsen et al. 2007; Mehner et al. 2010, 2012; Madura et al. 2012; Davidson et al. 2015). Additionally, it ionizes the inner 1″ circumstellar ejecta (Weigelt & Ebersberger 1986; Hofmann & Weigelt 1988; Weigelt et al. 1995). 2D radiative transfer models and 3D hydrodynamical simulations of the wind-wind collision scenario suggest that the high-velocity secondary wind penetrates the slower and denser primary wind creating a low-density cavity in it, with thin and dense walls where the two winds interact (Okazaki et al. 2008; Groh et al. 2012a; Madura et al. 2012, 2013; Clementel et al. 2015a,b). This wind-wind collision scenario produces the shock-heated gas responsible for the X-ray variability, and the ionization effects observed in the optical, infrared, and ultraviolet spectra.

These aforementioned models also show that during the periastron passage (phase $\phi \sim 0.98-1.02$) the acceleration zone of the post-shock wind of η_B is affected by η_A. The hot wind of η_B pushes the primary wind outward and it ends up trapped inside the cavity walls. The material in the walls is accelerated to velocities larger than η_A's wind terminal velocity, creating a layer of dense trapped primary wind. These layers have been observed as concentric fossil wind arcs in [Fe II] and [Ni II] images at the inner 1″ obtained with the HST/STIS camera (Teodoro et al. 2013; Gull et al. 2016).

To explain the wind-wind phenomenology at 2–10 mas (∼5–25 au) scales, several attempts have been made to characterize the core of η Car. Particularly, long-baseline infrared interferometry has been a decisive technique for such studies. Kervella et al. (2002) and van Boekel et al. (2003) resolved an elongated optically thick region using the *K*-band (2.0–2.4 μm) beam-combiner VINCI (Kervella et al. 2000) at the Very Large Telescope Interferometer (VLTI; Glindemann et al. 2003). Those authors measured a size of 5–7 mas (11–15 au) for η Car's core, with a major to minor axis ratio $\epsilon = 1.25 \pm 0.05$, and a PA = 134 ± 7°. Using a non-local thermal equilibrium (non-LTE) model, a mass-loss rate of $1.6 \pm 0.3 \times 10^{-3}\ M_\odot\ \mathrm{yr}^{-1}$ was estimated.

Follow-up observations (Weigelt et al. 2007) with the *K*-band beam combiner VLTI-AMBER (Petrov et al. 2007) using medium ($R = 1500$) and high ($R = 12\,000$) spectral resolutions of the He I 2s-2p (2.0587 μm) and Brγ (2.1661 μm) lines, resolved η Car's wind structure at angular scales as small as ∼6 mas (∼13 au). These authors measured a (50% encircled energy) diameter of 3.74–4.23 mas (8.6–9.7 au) for the continuum at 2.04 μm and 2.17 μm; a diameter of 9.6 mas (22.6 au) at the peak of the Brγ line; and 6.5 mas (15.3 au) at the emission peak of the He I 2s-2p line. They also confirmed the presence of an elongated optically thick continuum core with a measured axis ratio $\epsilon = 1.18 \pm 0.10$ and a projected PA = 120° ± 15°.

The observed non-zero differential phases and closure phases indicate a complex extended structure across the emission lines. To explain the Brγ-line profile and the signatures observed in the differential and closure phases, Weigelt et al. (2007) developed a "rugby-ball" model for an optically thick, latitude dependent wind, which includes three components: (a) a continuum spherical component; (b) a spherical primary wind; (c) and a surrounding aspherical wind component inclined 41° from the observer's LOS.

New high-resolution AMBER observations in 2014 allowed Weigelt et al. (2016) to reconstruct the first aperture-synthesis images across the Brγ line. These images revealed an asymmetric and elongated structure, particularly in the blue wing of the line. At velocities between −140 and −380 km s⁻¹, the intensity distribution of the reconstructed maps shows a fan-shaped structure with an 8.0 mas (18.8 au) extension to the southeast and 5.8 mas (13.6 au) to the northwest. The symmetry axis of this elongation is at a PA = 126°, which coincides with that of the Homunculus axis. This fan-shaped morphology is consistent with the wind-wind collision cavity scenario described by Okazaki et al. (2008), Madura et al. (2012, 2013), and Teodoro et al. (2013, 2016), with the observed emission originating mainly from the material flowing along the cavity in a LOS preferential toward the southeast wall.

Additionally to the wind-wind collision cavity, several other wind structures were discovered in the images reported by Weigelt et al. (2016). At velocities between −430 and −340 km s⁻¹, a bar-like feature appears to be located southwest of the continuum. This bar has the same PA as the more extended fossil wind structure reported by Falcke et al. (1996) and Gull et al. (2011, 2016), that may correspond to an equatorial disk and/or toroidal material that obscures the primary star in the LOS. At positive velocities, the emission appears not to be as extended as in the blue-shifted part of the line. This may be because we are looking at the back (red-shifted) part of the primary wind that is less extended because it is not as deformed by the wind collision zone. Finally, the wind lacks any strong emission line features at velocities lower than −430 km s⁻¹ or larger than +400 km s⁻¹.

This work presents VLTI-GRAVITY chromatic imaging of η Car's core across two spectral lines in the infrared *K*-band: He I 2s-2p and Brγ. The paper is outlined as follows: Sect. 2 presents our GRAVITY observations and data reduction. In Sect. 3 the analyses of the interferometric observables, and the details of the imaging procedure are described. In Sect. 4 our results are discussed and, finally, in Sect. 5 the conclusions are presented.

2. Observations and data reduction

2.1. Observations

The milliarcsecond resolution of GRAVITY (Eisenhauer et al. 2008, 2011; Gravity Collaboration 2017) enables spectrally resolved interferometric imaging of the central wind region of η Car. At an apparent magnitude of $m_K = 0.94$ mag, the target is bright enough for observations with the 1.8-m Auxiliary Telescopes (ATs). η Car was observed during the nights of February 24th and 27th, 2016, as part of the commissioning phase of the instrument, and during the nights of May 30th and July 1st 2017, as part of the GRAVITY Guaranteed Time Observations (GTO). The observations were carried out using the highest spectral resolution ($R = 4000$) of the GRAVITY beam combiner, together with the split-polarization and single-field modes of the instrument. With this configuration, GRAVITY splits the incoming light of the science target equally between the fringe tracker and science beam combiner to simultaneously produce interference fringes in both. While the science beam combiner disperses the light at the desired spectral resolution, the fringe tracker works with a low-spectral resolution of $R \sim 22$ (Gillessen et al. 2010) but at a high temporal sampling (∼1 kHz). This allows to correct for the atmospheric piston, and to stabilize the fringes of the science beam combiner.

For the 2016 observations, ten data sets were recorded with the A0-G1-J2-K0 array plus four more with the A0-G2-J2-J3 configuration. The *u*−*v* coverage obtained (Fig. 2) provides a maximum projected baseline of ∼130 m (J2-A0) that corresponds to a maximum angular resolution ($\theta = \lambda/2B$; where *B* is the maximum baseline) of $\theta = 1.75$ mas, at a central wavelength of $\lambda_0 = 2.2$ μm. The 2017 observations comprise three data sets with the D0-B2-J3-K0 array plus seven data sets with the A0-G1-J2-K0 array. For this second epoch the maximum baseline length (J2-A0) was around 122 m ($\theta = 1.85$ mas). However, since most of the longest baselines for both imaging epochs are of 100 m, we adopted a mean maximum angular resolution $\theta = 2.26$ mas for our imaging program. Tables A.1 and A.2 list individual data sets and observing conditions.

2.2. Data reduction

The interferometric observables (squared visibilities, closure phases, and differential phases) as well as the source's spectrum were obtained using versions 0.9.0 and 1.0.7 of the GRAVITY data reduction software[1] (Lapeyrere et al. 2014). More details on the data reduction procedure are provided in Sanchez-Bermudez et al. (2017). To calibrate the interferometric observables, interleaved observations of the science target and a point-like source were performed. We used the K3 II star HD 89682 (*K*-band Uniform Disk diameter $d_{UD} = 2.88$ mas) as interferometric calibrator for both epochs. Before analyzing the
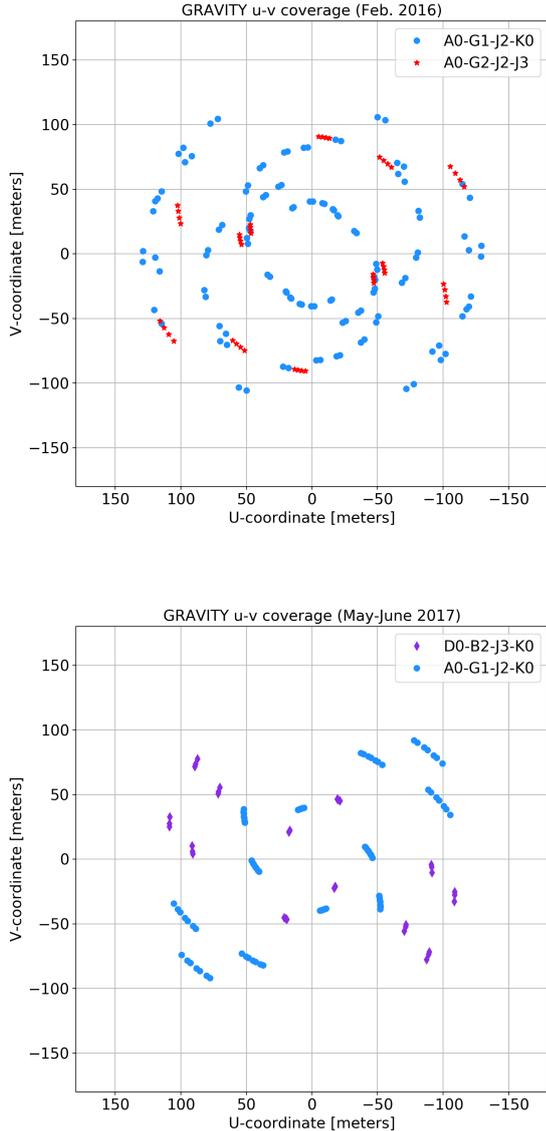
---

[1] http://www.eso.org/sci/software/pipelines/gravity/gravity-pipe-recipes.html

Fig. 2. η Car's *u*−*v* coverages obtained during the GRAVITY runs in February 2016 (*top panel*) and May-June 2017 (*bottom panel*). Different quadruplets are indicated with different colors.

data, all the squared visibility (V^2) points with a signal-to-noise ratio (S/N) ≤ 5 and closure phases with σ_{cp} ≥ 40° were excluded from the analysis.

2.3. Calibration of η Car's integrated spectrum

For each one of the data sets, four samples of η Car's integrated spectrum were obtained with GRAVITY. The data reduction software delivers the spectrum flattened by the instrumental transfer function obtained from the Pixel to Visibility Matrix (P2VM; Petrov et al. 2007). Additionally, GRAVITY uses the internal calibration unit (Blind et al. 2014) to obtain the fiber wavelength scale, producing a wavelength map with a precision of Δ_λ = 2 nm. Apart from this preliminary calibrations, we had to correct the η Car spectrum for the atmospheric transfer function together with a more precise wavelength calibration. For this purpose, we used the following method:

1. A weighted average science and calibrator spectra were computed from the different samples obtained with GRAVITY.

2. To refine the wavelength calibration, we used a series of telluric lines across the spectrum of our interferometric calibrator. A Gaussian was fitted to each one of the lines profiles recording their peak positions. The high-resolution (R = 40 000) telluric spectrum at the Kitt Peak observatory was then used as reference to re-calibrate the GRAVITY wavelength map. For this, we first degraded the reference spectrum to the GRAVITY resolution and then, we identified a mean wavelength shift of the calibrator's tellurics from the Kitt Peak ones. Finally, the GRAVITY wavelength map was corrected. With this method, we reached a 1σ wavelength calibration error relative to the reference spectrum of 1.23 Å ($\Delta\nu$ = 16.8 km s^{-1} at λ_0 = 2.2 μm) for the 2016 data, and 0.67 Å ($\Delta\nu$ = 9.1 km s^{-1}) for the 2017 data, respectively. A similar calibration method was used by Weigelt et al. (2007, 2016) on the previously reported η Car AMBER data.

3. Once the wavelength calibration was performed, we remove the atmospheric transfer function from the η Car spectrum by obtaining the ratio of the science target and of the interferometric calibrator spectra. Since the interferometric calibrator, HD 89682, is a K3 II star, we have to correct for its intrinsic photospheric lines (e.g., the CO bands seen in absorption from 2.29 μm onward). For this purpose, we used a theoretical BT-Settl[2] model (see Allard et al. 2012) of a star with a T_{eff} = 4200 K, a log(g) = 1.5, and Z = −0.5. Figure 3 displays the normalized η Car spectrum with all the lines, between 2.0 μm and 2.2 μm, with interferometric signals different from the continuum labeled. Although the 2016 spectrum appears to be slightly noisier than the 2017 one, no significant differences were found between the two GRAVITY epochs. This work focuses on the interferometric imaging of η Car across He I 2s-2p and Brγ. Figure 4 displays the normalized η Car spectrum at these wavelengths, together with the differential visibilities and phases of one of our interferometric data sets. Notice the strong changes of the observables between the continuum and the lines.

2.4. Ancillary FEROS spectrum

To complement the analysis of the η Car GRAVITY spectrum, we obtained four optical high-resolution spectra of the source using the Fiber-fed Extended Range Optical Spectrograph (FEROS; Kaufer & Pasquini 1998) at the MPG 2.2 m telescope at La Silla Observatory in Chile. FEROS covers the entire optical spectral range from 3600 Å to 9200 Å and provides a spectral resolution of R = 48 000. All spectra were obtained using the object-sky mode where one of the two fibers is positioned on the target star and the other fiber is simultaneously fed with the sky background. The exposure time was 15 s and 30 s for every two spectra. The reduction and calibration of the raw data were performed using the CERES pipeline (Brahm et al. 2017). Figure F.1 displays a normalized mean spectrum of the four samples.

3. Data Analysis

3.1. Geometric model to the GRAVITY Fringe Tracker data

To obtain an angular measurement of the continuum size, a geometrical model was applied to the V^2 Fringe Tracker data. The model consists of two Gaussian disks with different angular sizes
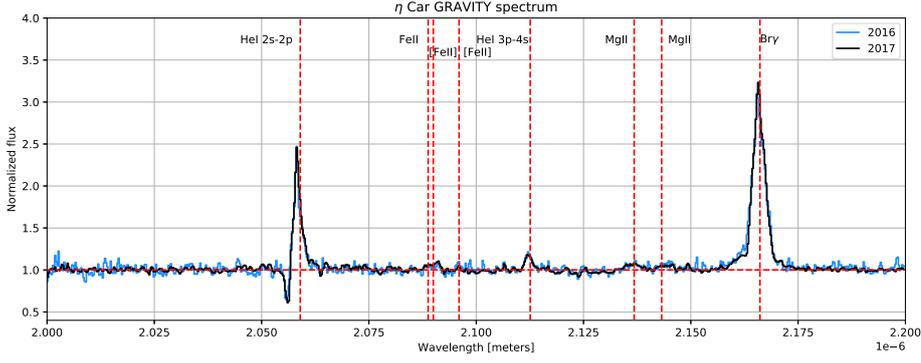
---

2 http://svo2.cab.inta-csic.es/theory/newov2/

Fig. 3. 2016 (blue straight line) and 2017 (black straight line) η Car normalized spectra in the 2.0–2.2 μm bandpass. The vertical red-dashed lines indicate the spectral features identified in the spectrum.
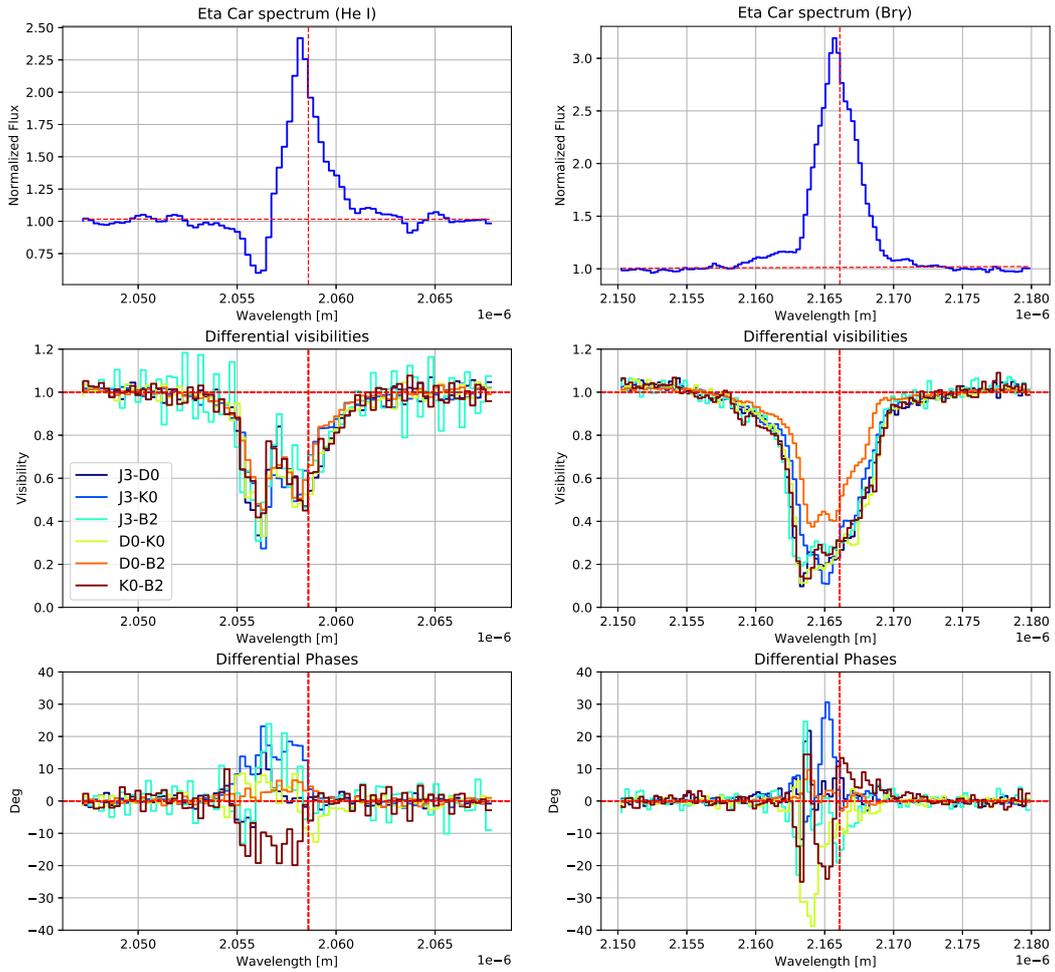

Fig. 4. Normalized GRAVITY spectrum at the position of the He I 2s-2p and Brγ lines. The calibrated differential visibilities (*middle*) and phases (*bottom*) of one of the GRAVITY data sets (MJD: 57903.9840) are also shown. In the *middle* and *bottom panels*, different colors correspond to each one of the baselines in the data set (see label on the plots). The dashed-red vertical lines indicate the reference wavelength of the emission feature, and the dashed-horizontal lines show the reference value of the continuum baseline.

tracing the compact and extended brightness distribution of the source. The expression used to estimate the complex visibilities, $V(u, v)$, is the following one:

$$V(u, v) = \frac{G(\theta_1, u, v) + F_2/F_1 G(\theta_2, u, v)}{1 + F_2/F_1} \qquad (1)$$

with

$$G(\theta, u, v) = \exp\left(\frac{-\pi\theta \sqrt{(u^2 + v^2)}}{4\ln(2)}\right), \qquad (2)$$

where F_2/F_1 is the flux ratio between the two Gaussian disks, (u, v) are components of the spatial frequency sampled per each observed visibility point ($u = B_x/\lambda$ and $v = B_y/\lambda$), and θ is the fitted full-width-at-half-maximum (FWHM) angular size for each one of the components.

Since previous studies suggest an elongation of η Car's core along the projected PA of the Homunculus semi-major axis, we applied our geometrical model to V^2 at two orientations. To cover PAs perpendicular and parallel to the semi-major axis of the nebula, we used all the V^2 points at $PA_\perp = 40° \pm 20°$ and at $PA_\parallel = 130° \pm 20°$, respectively. The model optimization was
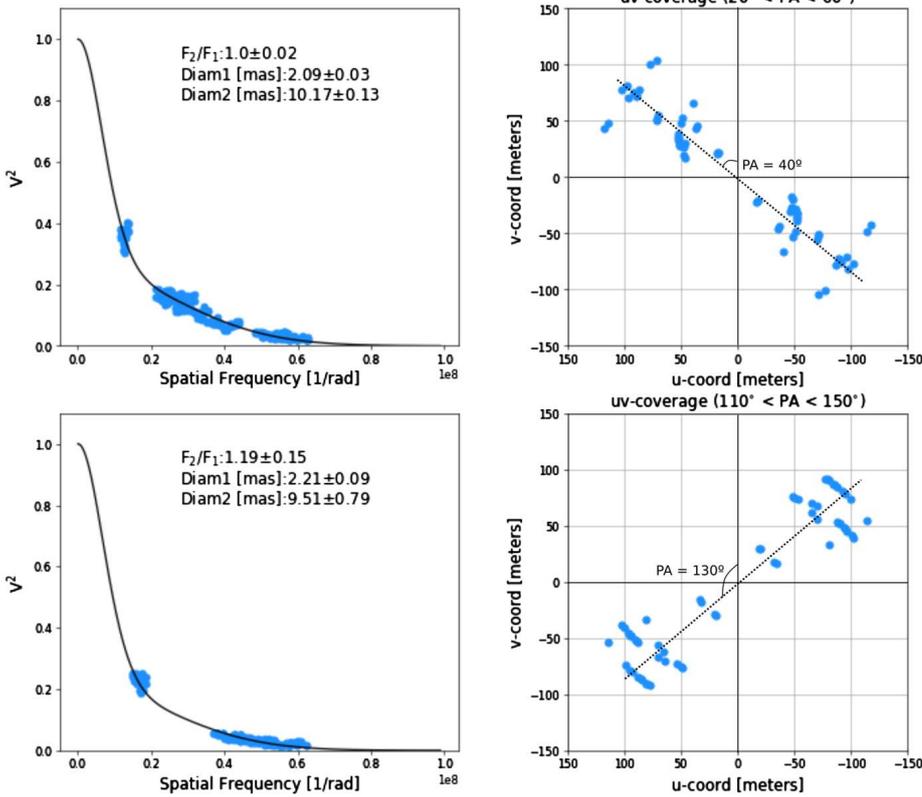
Fig. 5. *Left panels*: best-fit geometrical model to the Fringe Tracker V^2 data. The model is plotted with a black line, the data are shown with blue dots and the model parameters (with their uncertainties) are indicated on each panel. *Right panels*: visibility points used for each model fitting at two different position angles, $PA_{\perp} = 40° \pm 20°$ and $PA_{\parallel} = 130° \pm 20°$.

Table 1. Best-fit parameters of the geometrical model.

PA	Parameter	Value	$1-\sigma$
$40° \pm 20°$	θ_1 [mas]	2.09	0.03
	θ_2 [mas]	10.17	0.13
	F_2 / F_1	1.00	0.02
$130° \pm 20°$	θ_1 [mas]	2.21	0.09
	θ_2 [mas]	9.51	0.79
	F_2 / F_1	1.19	0.15

done using a dedicated Markov-Chain Monte-Carlo (MCMC) routine based on the python software pymc (Patil et al. 2010). To account for the standard deviations and correlations of the model parameters, we explore the solution space over 10 000 different models, considering the first 5000 iterations as part of the burn-in phase and accepting only one every three draws of the Monte Carlo. Initial linear distributions were assumed for all the parameters. To avoid an underestimation of the error-bars, the waist of the posterior Gaussian likelihood distribution was also marginalized for each one of the fitted parameters. Figure 5 shows the best-fit model and its uncertainties. Table 1 displays the best-fit parameters of our geometrical model and Figure B.1 shows the 2D posterior distributions of the fitted parameters.

3.2. Image reconstruction of the science beam combiner data

3.2.1. Chromatic reconstruction: Brγ and He I

The high accuracy of the interferometric observables allows a chromatic image reconstruction of η Car across the Brγ

and He I 2s-2p lines. For this purpose, we used SQUEEZE[3] (Baron & Kloppenborg 2010), an interferometry imaging software that allows simultaneous fitting of the visibility amplitudes, squared visibilities, closure phases, and chromatic differential phases (or combinations of them). At infrared wavelengths, image reconstruction from interferometric data is constrained mainly by the (i) sparse baseline coverage and (ii) lack of absolute phase information. Therefore, SQUEEZE applies a regularized minimization of the form:

$$x_{\mathrm{ML}} = \underset{x}{\mathrm{argmin}}[1/2\chi^2(x) + \sum_{i}^{n} \mu_i R(x)_i],\qquad(3)$$

where $\chi^2(x)$ is the likelihood of our data to a given imaging model, $R(x)_i$ are the (prior) regularization functions used and μ_i the weighting factors that trade-off between the likelihood and priors. For η Car, we used a combination of the following three different SQUEEZE regularizers:

1. To avoid spurious point-like sources in the field-of-view (FOV), we applied a spatial L0-norm.
2. To enhance the extended structure expected in some of the mapped spectral channels, a Laplacian was used.
3. To ensure spectral continuity all over the mapped emission lines, a spectral L2-norm was applied.

For the minimization, SQUEEZE uses a Simulated Annealing Monte-Carlo algorithm as the engine for the reconstruction. We created 15 chains with 250 iterations each to find the most probable image that best-fit our interferometric data. We used a 67×67 pixel grid with a scale of 0.6 mas/pixel. As initial point for the reconstruction, we chose a Gaussian with a FWHM of 2 mas centered in the pixel grid, and containing 50% of the total flux. We simultaneously fitted the V^2, closure phases, and wavelength-differential phases. The differential phase is defined in SQUEEZE
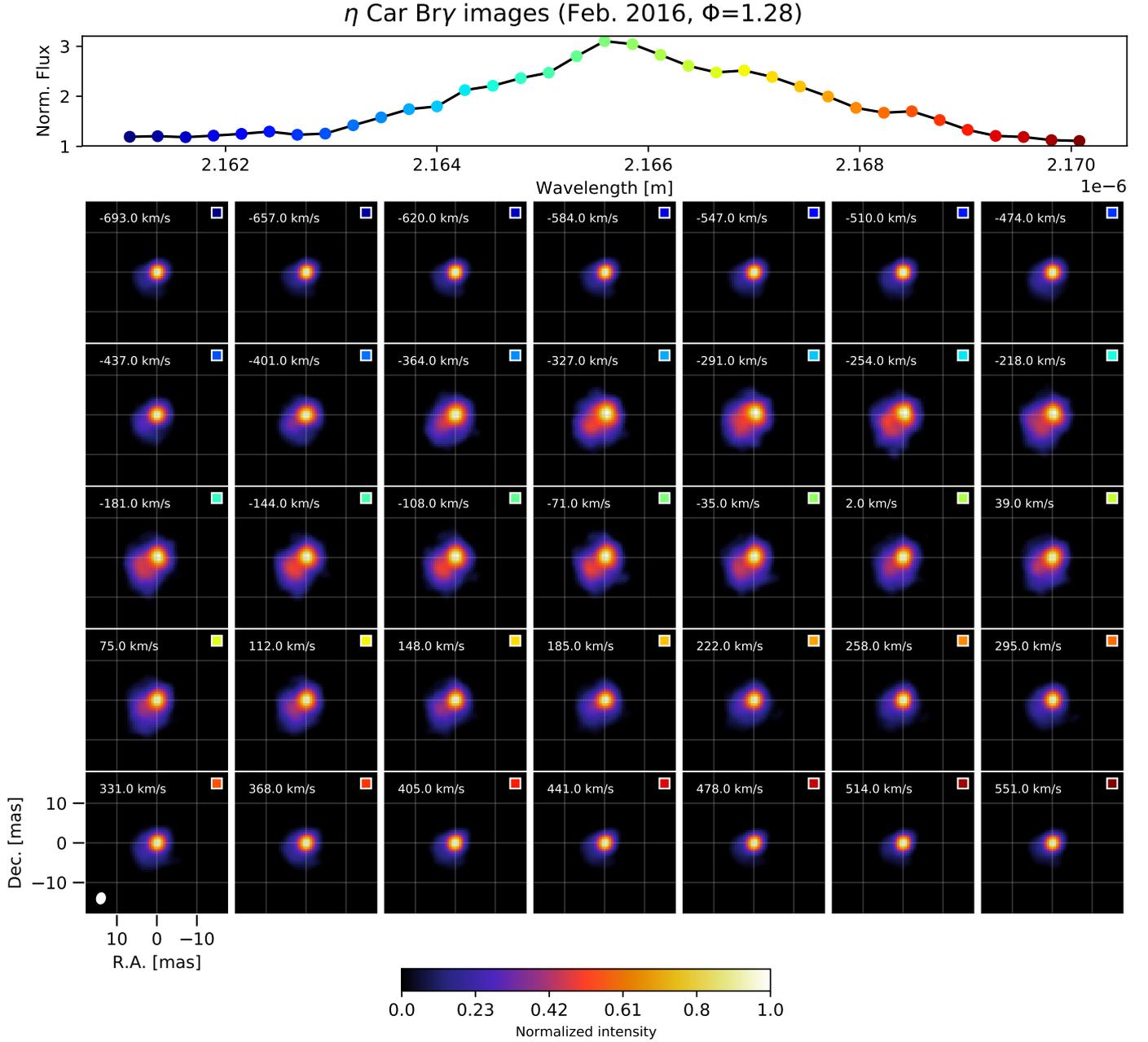
---

[3] https://github.com/fabienbaron/squeeze

η Car Brγ images (Feb. 2016, Φ=1.28)

Fig. 6. Brγ interferometric aperture synthesis images from the Feb. 2016 data. The Doppler velocity of each frame is labeled in the images. For all the panels, east is to the left and north to the top. The displayed FOV corresponds to 36×36 mas. The small white ellipse shown in the *lowermost-left panel* corresponds to the synthesized primary beam (the detailed PSF is shown in Fig. D.1). Above all the images, the GRAVITY spectrum is shown and the different positions where the images are reconstructed across the line are labeled with a colored square, which is also plotted in the images for an easy identification.

of the following form:

$$\phi(\lambda_i) = \phi_0(\lambda_i) - \phi_{ref}. \tag{4}$$

where $\phi_0(\lambda_i)$ is the measured phase at channel i, and ϕ_{ref} is the reference phase. The `SQUEEZE` implementation of $\phi(\lambda_i)$ uses the `REFMAP` table, of the `OI_VIS` extension in the `OIFITS v2` files (Pauls et al. 2005; Duvert et al. 2017), to determine which channels are used to define the reference phase ϕ_{ref}. In our case, we defined ϕ_{ref} as the average of the measured phases over the full spectral bandpass used for the reconstruction, with exception of the working channel itself, in the following way:

$$\phi_{ref} = \langle\phi_0(\lambda_k)\rangle_{\lambda_k \neq \lambda_i} \tag{5}$$

With this definition, the reference phase varies from channel to channel but avoids quadratic bias terms (a similar definition of $\phi(\lambda_i)$ has been used before to analyze AMBER data; see e.g., Millour et al. 2006, 2007; Petrov et al. 2007). While the V^2 data measure the flux contribution at different spatial scales and the closure phases the asymmetry of the source, the wavelength-differential phases give information about the relative flux-centroid displacement between a given wavelength and the reference one.

For Brγ, 35 channels between 2.160 μm and 2.171 μm were imaged, while for He I, 34 channels between 2.054 μm and 2.063 μm were used. The final mean images were created through the following procedure:

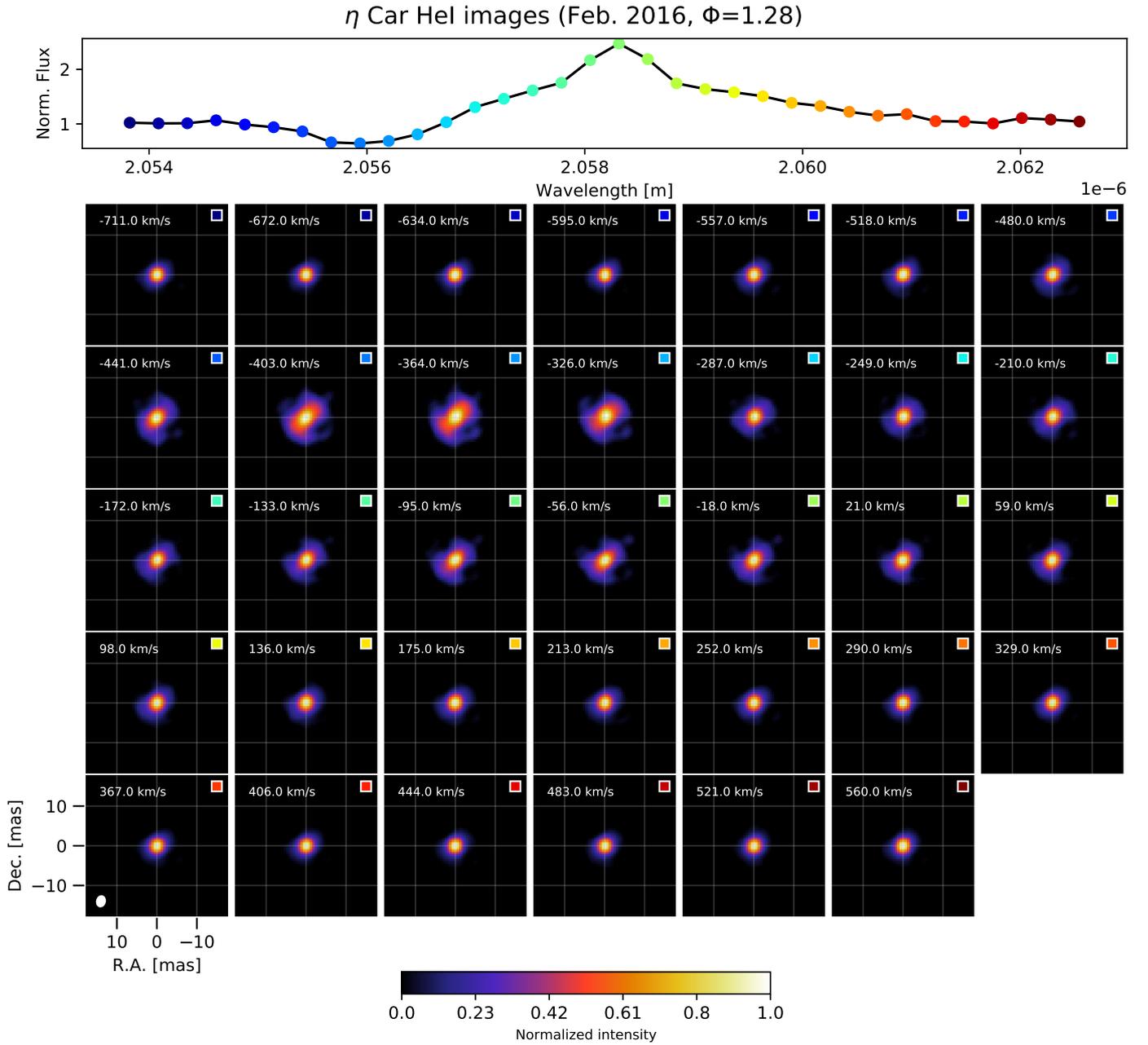## η Car HeI images (Feb. 2016, Φ=1.28)

Fig. 7. He I interferometric aperture synthesis images from the Feb. 2016 data. The maps are as described in Fig. 6.

1. We ranked the converged chains, assigning the highest score to the one with the global χ^2 closest to unity. From the ranked chains, we select the best five of them to create the final images.
2. To align the selected cubes of images to a common reference pixel position, a mean centroid position of the continuum was estimated. For this purpose, the first and last five channels of each cube of images were used. The individual centroid positions were computed using a mask of five pixels around the maxima of the images at every channel used as continuum reference. Then, their mean value was computed. All the images in the cube were shifted, with sub-pixel accuracy ($\sim$0.1 pixels), from this mean centroid position to the center of the image defined at position [34,34] in the pixel grid.
3. From the aligned cubes, we compute a mean image per wavelength. Finally, since most of the spatial frequencies in the $u-v$ coverages correspond to 100 m baselines, each image

was smoothed with a 2D Gaussian with a FWHM equivalent to $\lambda_0/2B_{\mathrm{max}} = 2.26$ mas.

For both lines, reconstruction tests with the s- and p-polarization data were done independently, however, no significant morphological changes were observed. The images here presented correspond to the p-polarization data. Figures 6 and 7 show the mean-reconstructed 2016 Brγ and He I images, respectively. The 2017 images are shown in Figs. D.1 and D.2. To inspect the quality of the reconstruction, Figs. E.1–E.8 display the V^2 and closure phases from the recovered images together with the data.

3.2.2. Effects of the $u-v$ coverage on the reconstructed images

Due to the interacting winds of the eccentric binary at the core of η Car, we expect changes in the spatial distribution of the flux
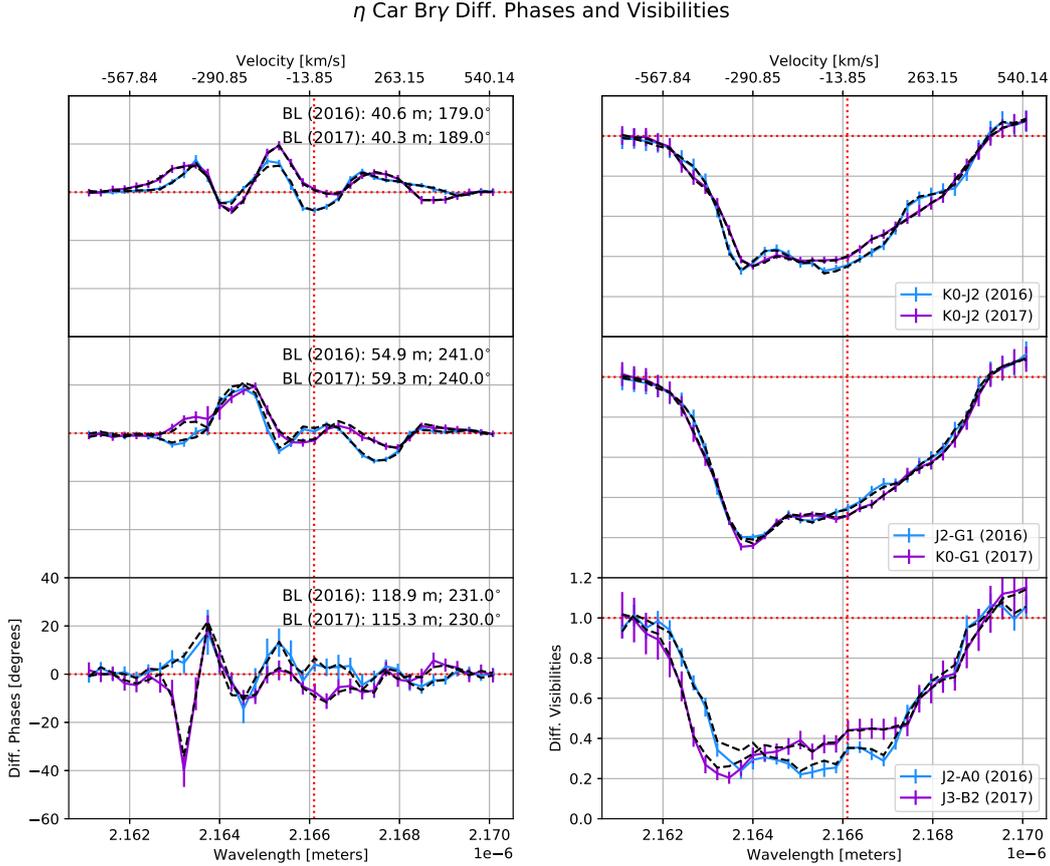
Fig. 8. Differential phases (*left panels*) and differential visibilities (*right panels*) between the continuum and the line emission for the 2016 (blue line) and 2017 data (purple line). The (reference) continuum phase and visibility were estimated using the first and last five channels in the imaged bandpass. Each one of the rows corresponds to a similar baseline in both epochs, tracing large (*top*), intermediate (*middle*) and small (*bottom*) spatial scales. The baseline lengths and position angles are labeled on the *left panels*, while the baseline stations are labeled on the *right* ones. The black-dashed lines correspond to the differential quantities extracted from the unconvolved reconstructed images. The vertical red-dotted line marks the systemic velocity of Brγ. The horizontal red-dotted lines show the continuum baselines.

at different orbital phases. This condition could explain the differences in the observed morphologies between our two imaging epochs. However, while the $u-v$ coverage of the 2016 data is homogeneous, the 2017 $u-v$ coverage is more sparse. The sparseness of the 2017 $u-v$ coverage was caused, partially, because the target was observable above 35° over the horizon only for a few hours at the beginning of the night.

Therefore, the long baselines of our interferometric array could not properly sample north-south orientations of the $u-v$ space. This sparseness in the $u-v$ coverage produced a clumpy fine structure and a cross-like shape, superimposed on the source's emission, on the reconstructed images. This cross-like structure is caused by the strong secondary lobes and the elongation of the primary beam (see Fig. C.1). This effect could mimic or mask real changes in the morphology associated with the physics of the wind-wind interactions with the synthesized beam and/or artifacts in the reconstruction process.

To detect the morphological changes between two epochs associated to the physical conditions of the source and not caused by the $u-v$ coverage, we searched for coincidental baselines (in size and position angle) at both epochs, to compare the differential phases and visibilities between them. This test allows us to monitor the flux centroid evolution between the continuum and the lines together with the changes observed in the flux distribution. Three baselines, tracing the small, intermediate and

large angular scales were selected. Additionally, we compute the differential observables from the reconstructed images to monitor the goodness of the images recovering the possible morphological changes.

Figure 8 displays, as an example, the results of this comparison for Brγ. For the short ($\theta = 5.7$ mas; 13.4 au) and intermediate ($\theta = 3.8$ mas; 8.4 au) baselines, the overall signatures of the centroid and of the flux distribution are similar at both epochs, with more prominent centroid changes at blue-shifted velocities than at the red-shifted side. The long ($\theta = 1.9$ mas; 4.46 au) baseline shows more drastic differences at blue-shifted velocities between the two epochs. For example, while the differential phases of the 2017 data exhibit an upside-down double-peak profile at velocities between -420 km s^{-1} and -170 km s^{-1}, the 2016 shows a single and less prominent peak.

These changes in the observables for coincidental baselines provide evidence of modifications in the brightness distribution between the two epochs. However, despite the good fit of the 2017 images to the observables (see Figs. E.3, E.4, E.7, and E.8), it is clear that the sparse $u-v$ coverage of the second epoch strongly detriments the quality of the reconstructed images. Therefore, they cannot be used for a proper (direct) comparison of the global morphology observed in the 2016 data. Thus, the 2017 images were excluded for the following analysis and discussion.

Table 2. Stellar parameters of the CMFGEN models.

Parameter	Groh et al. (2012a)	This work
$T_{\rm eff}$	9.4 kK	13.5 kK
$\log(L/L_\odot)^a$	6.7	7.1
Y^b	0.55%	0.50%
$\log(\dot{M}/M_\odot/{\rm year})$	-3.1	-3.4
β^c	1.0	1.0
$f_{\rm v}^d$	0.1	0.1
v_∞^e	420 km s^{-1}	420 km s^{-1}

Notes. β, $f_{\rm v}$, and v_∞ were fixed parameters in our grid of models. The used values were taken from Groh et al. (2012a). $^{(a)}\log(L/L_\odot)$ is scaled to match the K-Band flux. $^{(b)}$Helium abundance in mass fraction. $^{(c)}$Exponent of the wind-velocity law. $^{(d)}$Volume filling factor. $^{(e)}$Stellar wind's terminal velocity.

4. Discussion

4.1. Spectroscopic analysis of η Car's primary wind

To characterize the properties of $\eta_{\rm A}$'s wind, we fitted the integrated spectrum of our GRAVITY observations (Sect. 2.3) with model spectra. The synthetic spectra were computed with the 1D spherical non-LTE stellar atmosphere and radiative transfer code CMFGEN (Hillier & Miller 1998). Our atomic model includes a large number of ionization stages to cover a wide temperature range in our stellar atmosphere grid without changing the atomic model. The following ions were taken into account: H I, He I-II, C I-IV, N I-IV, O I-IV, Ne I-IV, Na I-IV, Mg I-IV, Ca I-IV, Al I-IV, Si I-IV, P II-V, S I-V, Ar I-IV, Fe I-V, and Ni II-V; and the metallicity was set to solar according to Asplund et al. (2005). For comparison, we computed a reference spectrum with the stellar parameters derived by Groh et al. (2012a) for the primary, which in turn is based on previous estimates by Hillier et al. (2001, 2006). The terminal velocity (v_∞), beta-type velocity law (β) and volume-filling factor ($f_{\rm v}$) were taken from Groh et al. (2012a) and were not varied for the grid computation. The luminosity was scaled to match the K-band flux of the reference spectrum. The stellar parameters of our best-fit model and the reference spectrum are listed in Table 2.

While our best-fit model reproduces the spectral lines in the GRAVITY spectrum between 2.0 μm and 2.2 μm, the reference spectrum fails to reproduce the He I lines (Fig. 9). Our best-fit model is about 4000 K hotter than the reference spectrum, but the mass-loss rate is decreased by a factor of two. There is a large debate in the literature whether $\eta_{\rm A}$'s mass-loss rate has decreased by a factor between two to four over the last two decades (see e.g., Corcoran et al. 2010; Mehner et al. 2010, 2012, 2014). This could explain the change in the mass-loss estimate from the 2000 HST data used by Groh et al. (2012a) and our 2016–2017 GRAVITY observations, but not the increased temperature.

However, this scenario is not fully consistent with all the observational evidence and theoretical predictions. The hydrodynamic simulations of the wind-wind collision zone, created by Madura et al. (2013), suggest that, instead of an extreme decrease of the $\eta_{\rm A}$ mass-loss rate, changes in η Car's ultra-violet, optical, and X-ray light curves, as well as of the spectral features, are due to slight changes in the wind-wind collision cavity opening angle in combination with a moderate change in the mass-loss rate.
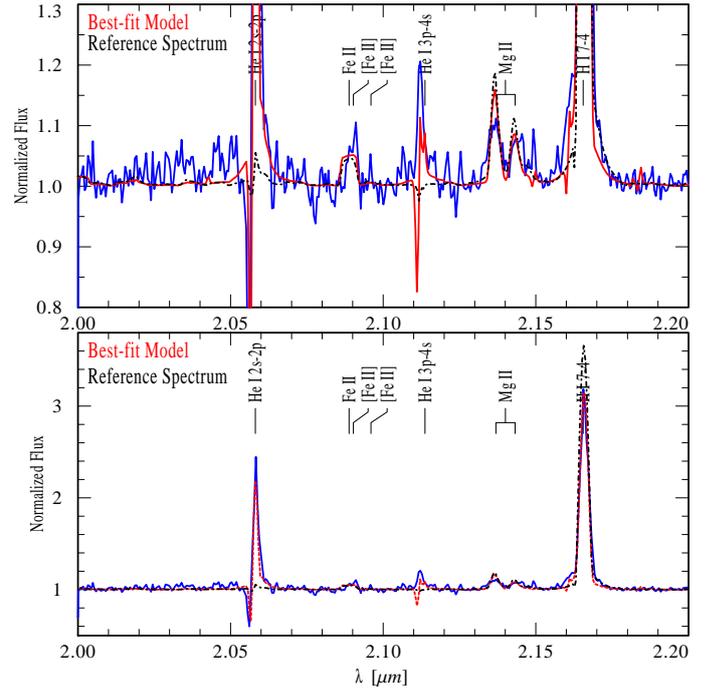

Fig. 9. *Lower panel*: GRAVITY spectrum from 2.0 μm to 2.2 μm (blue-solid line) with a vertical scale that displays the complete line profiles. *Upper panel*: magnification of the GRAVITY spectrum, where the fine details of our best-fit CMFGEN model (red-dashed line) and of the reference spectrum derived with the stellar parameters from Groh et al. (2012a) (black-dashed line) are appreciated. Notice that the He I 2s-2p and He I 3p-4s are only matched by our hotter red model.

Moreover, when comparing our CMFGEN model with our complementary FEROS optical spectrum (λ4200–7100 Å), we noticed that it is not able to reproduce the metallic [Fe II] and Si II lines, while the cooler Groh model reproduces them (see Fig. F.1). Similar behavior is observed for other previous models that include low primary mass-loss rates close to $\sim 10^{-4}\ M_\odot$ yr^{-1} (see e.g., Fig. 12 in Madura et al. 2013). This speaks against the strong decrement in the mass-loss rate obtained by our CMFGEN model, and highlights that $\eta_{\rm B}$ plays a major role in the formation of the observed lines in the GRAVITY spectrum. The effects of the secondary and the wind-wind collision zone on the formation of Brγ and He I cannot be reflected by our 1D non-LTE single star model. Nevertheless, they can be investigated with aperture-synthesis images.

For a better understanding of the system's geometry and how $\eta_{\rm B}$ could change the parameters derived by our CMFGEN model, we show in Fig. 10 the line-forming regions of our best-fit model and of the reference one as a function of radius for He I 2s-2p (top panel) and Brγ (lower panel). The vertical black lines indicate the following reference points: (a) the red-dotted line shows the location of photosphere of $\eta_{\rm A}$, which is not equal to the hydrostatic radius (because of its optically thick wind) but to the point where the optical depth $\tau = 2/3$; (b) the black-solid line shows the mean angular resolution limit of the GRAVITY observations ($\sim$2 mas); (c) and the black-dashed line marks the expected projected position of $\eta_{\rm B}$ at the time of apastron.

With our CMFGEN model, the wind of $\eta_{\rm A}$ could form the peak of the Brγ emission only at 3 mas (7 au), which is clearly closer than the extended emission observed in the reconstructed images. Furthermore, it can be seen that, with a single star, the peak of the He I 2s-2p line is formed at an angular scale close
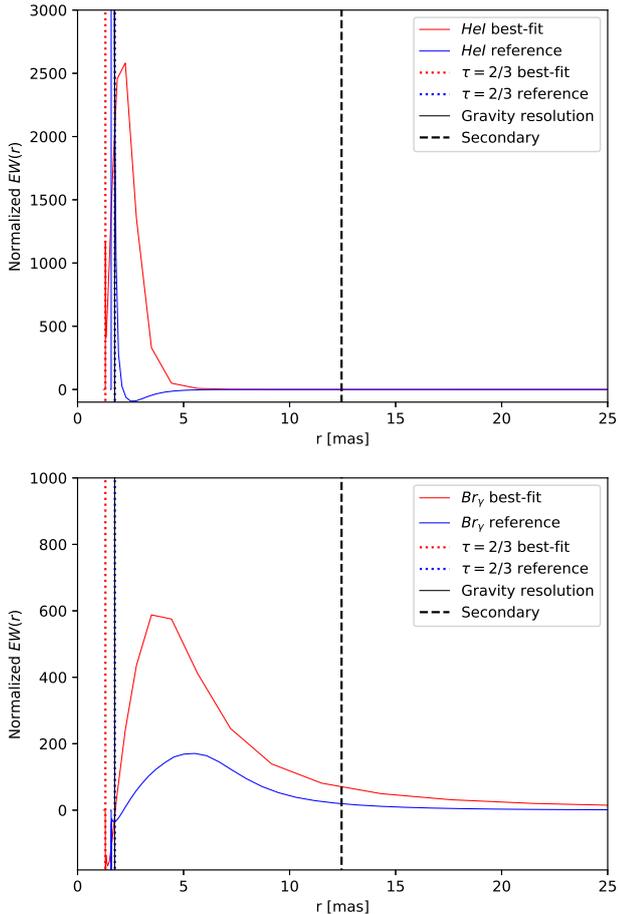
Fig. 10. CMFGEN normalized line equivalent width (EW) as a function of radius for our best-fit model and the reference one. *Top* and *bottom* *panels*: line-forming region as a function of radius for He I 2s-2p and Brγ, respectively. The red/blue dotted line corresponds the location of the η_A's photosphere. The black-solid line indicates the spatial resolution limit of GRAVITY and the black-dashed line shows the projected position of η_B at apastron, according with the mean orbital solution presented by Teodoro et al. (2016).

the resolution of our observations (in the reference model, the He I line-formation region is at a scale smaller than the resolution of GRAVITY). Therefore, the extended emission in the He I 2s-2p images should be related to the UV ionization of η_B on the wind-wind collision zone. Any modification to He I as a consequence of the wind-wind interaction would require that (i) η_B's wind penetrates deeply into the denser regions of the primary wind and/or (ii) that η_B ionizes part of the pre- and post-shock primary wind near the apex of the wind-wind collision zone. In this scenario, it is expected that the modification of the ionization structure caused by the secondary largely changes the intensity of Helium and Hydrogen lines depending on the orbital phase, particularly at periastron (see e.g., Groh et al. 2010a; Richardson et al. 2015, 2016).

We do not detect any significant differences in the line profiles between the 2016 and 2017 GRAVITY spectra. However, when comparing the 2016 GRAVITY data and the 2004 AMBER data reported by Weigelt et al. (2007) (both of them obtained at a similar orbital phase), we noticed that the He I 2s-2p shows the P-Cygni profile, but the amplitudes of the valley and peak are different for both data sets. This observation suggests the presence of a dynamical wind-wind collision environment with possible changes in the wind parameters over time (see e.g.,

Fig. 3 in Richardson et al. 2016, where the P-Cygni profile of He I λ5876 is observed close to several periastron passages but the profile of the line varies with time even for similar phases). Therefore, this highlights the importance of monitoring the lines' morphological changes through the reconstructed interferometric images.

4.2. The size of η Car's continuum emission

The observed quiescent continuum emission in η Car is caused by extended free-free and bound-free emission (Hillier et al. 2001), and it traces the dense, optically thick primary wind. From our geometrical model to the Fringe Tracker data, we estimated that ~50% of the K-band total flux corresponds to $\theta_{FWHM} = 2$ mas (~5 au) core (compact emission), with the rest of the flux arising from a surrounding halo of at least $\theta_{FWHM} = 10$ mas (~24 au; see Table 1). The size derived for the continuum η_A wind is consistent with the size of the extended primary photosphere, according with our CMFGEN model and previous spectroscopic and interferometric estimates (Hillier et al. 2001, 2006; Kervella et al. 2002; van Boekel et al. 2003; Weigelt et al. 2007, 2016).

Previous interferometric studies suggested an elongated continuum primary wind along the PA of the Homunculus. From our data modeling, we derived an elongation ratio of $\epsilon = 1.06 \pm 0.05$, a value that is consistent with the most recent interferometric measurements with AMBER, but it is $4-\sigma$ smaller than the first VINCI estimate in 2003 (see Table 3). It has been hypothesized that the origin of this elongation could be (i) a latitude-dependent wind caused by a rapid rotation of the primary and/or (ii) a consequence of the wind-wind collision cavity. For example, Mehner et al. (2014) suggest that the angular momentum transfer between η_A and η_B at periastron could be affected by tidal acceleration, resulting in a change of the rotation period of η_A, which in turn may affect the shape of the continuum emission.

Additionally, Groh et al. (2010a) used radiative transfer models applied to the VINCI and AMBER data to explore the changes in the continuum associated with modifications in the rotational velocity and with a "bore-hole" effect due to the presence of the wind-wind collision zone. These authors found that both prolate or oblate rotational models reproduce the interferometric signatures. Nevertheless, those models required large inclination angles in which η_A's rotational axis is not aligned with that of the Homunculus. Inclinations where the rotational axis is aligned with the Homunculus would require a decrement in the rotational velocity (and of the size) of η_A with time. However, the cavity could also mimic the effects of the observed elongation. Therefore, new radiative transfer models of interferometric data (including GRAVITY and other wavelengths like PIONIER in the H-band) are necessary to test these scenarios. Such models are beyond the scope of the present work and are left for future analysis.

4.3. The Brγ interferometric images in the context of the η Car wind-wind collision cavity

Our 2016 GRAVITY Brγ aperture-synthesis images reveal the morphology of η Car's wind-wind collision cavity. Here, we discuss the principal wind components and their interpretation with previous theoretical models and simulations. The Brγ maps reveal the following general structure as function of the radial velocity:

(1) Continuum wind region. For radial velocities smaller than -510 km s^{-1} and larger than $+368$ km s^{-1}, the maps show a

Table 3. Values of η Car's continuum elongation ratio from different interferometric observations.

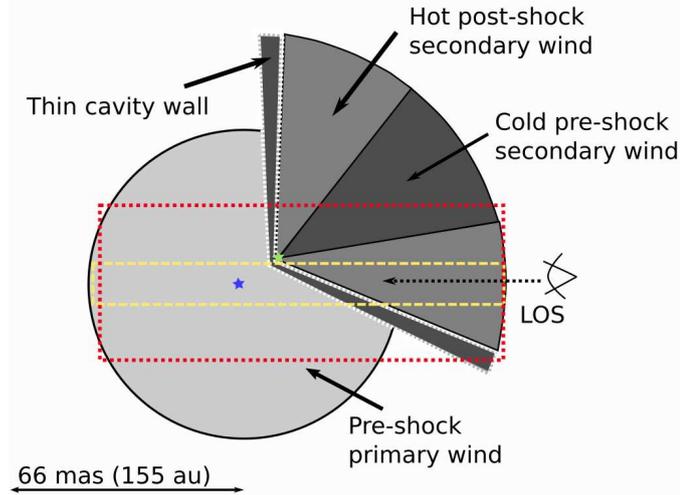| Reference	Instrument	Elongation ratio	PA
van Boekel et al. (2003)	VINCI	1.25 ± 0.05	$134° \pm 7°$
Weigelt et al. (2007)	AMBER	1.18 ± 0.10	$120° \pm 15°$
Weigelt et al. (2016)	AMBER	1.07 ± 0.14	$159° \pm 47°$
This work	GRAVITY	1.06 ± 0.05	$130° \pm 20°$

Fig. 11. Schematic of η Car's wind-wind collision scenario reported by Madura et al. (2013). The wind-wind collision cavity carved by the secondary (green star) in the primary wind is depicted, with the different elements of the primary (blue star) and secondary winds labeled. Notice how the LOS lies preferentially toward the lower cavity wall. The angular scales (centered around η_A) traced with the shortest baselines of the GRAVITY (~ 40 m) and AMBER (~ 10 m) data are shown with a yellow-dashed and red-dotted rectangles, respectively.

compact emission where the optically thick continuum wind region is dominant. For velocities between -510 km s^{-1} and $+368$ km s^{-1}, additional wind components are observed in the images, however, the continuum emission is always present.

(2) Wind-wind collision region. 3D smoothed particle hydrodynamic models (Okazaki et al. 2008; Gull et al. 2009; Madura et al. 2012, 2013; Teodoro et al. 2013, 2016) of η Car's wind-wind interaction suggest a density distribution that extends far beyond the size of the primary wind. This wind-wind collision zone is identified with a cavity created by the fast wind of η_B that penetrates deep into the dense but slow wind of η_A as the secondary changes its orbital phase. Following the orbital solution of Teodoro et al. (2016) presented in Fig. 1, η_B was close to apastron (in front of η_A) at the time of our GRAVITY observations. Figure 11 displays a schematic view of this wind-wind scenario according to Madura et al. (2013). The diagram represents the position of the system at apastron in a plane defined by the LOS and the sky plane (i.e., called the xz plane in Madura et al. 2013). The cavity opens with a LOS oriented preferably toward the southern wall, along its walls the hot ($T \sim 10^6$ K) post-shock η_B wind is moving, and, in between, the cold ($T \sim 10^4$ K) pre-shock η_B wind is observed.

In the Brγ GRAVITY images at radial velocities > -364 km s^{-1}, we observe an extended asymmetric emission increasing in size and brightness as we approach the systemic velocity, and then it decreases toward positive ones. At velocities between -364 km s^{-1} and -71 km s^{-1}, the wind-wind

collision cavity presents an elongated and asymmetric cone-like morphology with a bright arc-like feature in the southeast direction. The extended and bright southeast asymmetric emission was first observed in the AMBER images reported by Weigelt et al. (2016). In particular, for velocities between -140 km s^{-1} and -380 km s^{-1}, those authors identified a SE fan-shaped morphology. However, there are some changes between the AMBER images and the maps recovered with GRAVITY. We infer that some of those changes are associated with the dynamics of the wind-wind collision zone (i.e., different orbital phases), however, some others are caused by the different spatial frequencies sampled with the two observations.

The majority of the longest baselines of the AMBER data are of 80 m, which limits the angular resolution up to $\lambda/2B_{max} = 3$ mas, in contrast our GRAVITY data provide a mean maximum angular resolution of 2.26 mas. However, the AMBER data include a better sampling of low spatial frequencies with baselines as small as 10 m. In this respect, our GRAVITY data present a clear limitation since most of our short baselines are above 40 m. Those constraints allowed us to recover images of the small-scale structure of η Car, at the cost of restricting the imaging capabilities to map the most extended emission observed in the AMBER images.

Madura et al. (2013) suggested that the time-dependent changes in the spectral lines are a consequence of changes in the line-of-sight morphology of the wind-wind collision cavity. Their hydrodynamical simulations predict that, at apastron, the cavity maintains an axisymmetric conical shape with the leading and trailing arms clearly visible in the orbital plane[4]. The half-opening angle of the cavity depends on the ratio of the wind momenta, which can be expressed in terms of mass-loss rate and wind velocity ($\beta = \dot{M}_{\eta_A} v_{\eta_A} / \dot{M}_{\eta_B} v_{\eta_B}$), of the two interacting stars. Therefore, any modification to the mass-loss rates and/or wind velocities would change the opening angle of the cavity. For example, $\dot{M}_{\eta_A} = 8.5 \times 10^{-4} M_\odot$ yr^{-1} would produce a half-opening angle close to 55°. On the other hand, $\dot{M}_{\eta_A} = 1.6 \times 10^{-4} M_\odot$ yr^{-1} would create a half-opening angle close to 80°.

As η_B moves from apastron (lower-left panel in Fig. 12) toward the periastron, the wind-wind cavity is distorted, creating a spiral (lower-middle panel in Fig. 12). Interesting is the phenomenology after the periastron passage, where the leading arm of the cavity collides with the "old" trailing arm, forming a dense, cold, and compressed "shell" of η_A's wind (lower-right panel in Fig. 12). Since the secondary wind is providing pressure from the direction of the binary, but because of the very high velocity, the shell is expanding outward through the low-density region on the far (apastron) side, the expansion velocity could reach values larger than the terminal velocity of η_A's wind ($v_\infty = 420$ km s^{-1}). The stability and size of the com-

---

[4] For a complete description of the changes in the wind-wind collision cavity and their 3D orientation at scales relevant to the interferometric images, we refer the reader to Figs. 1, 2, B1, B2, B3 and B4 in Madura et al. (2013).
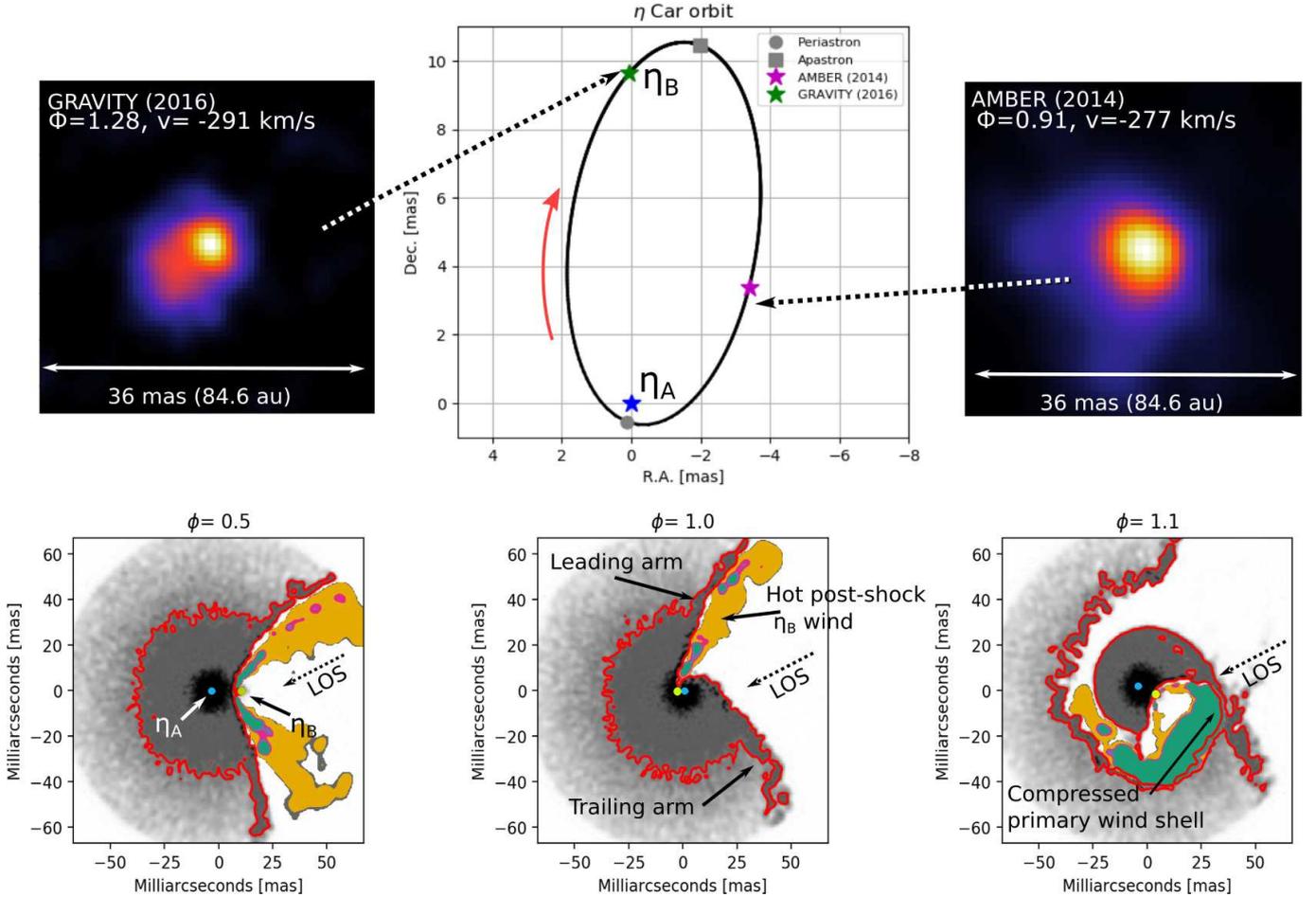
Fig. 12. *Upper-middle panel*: projected orbit of η_B around η_A, with the position of the periastron, apastron, and two imaging epochs labeled on it. *Upper-right panel*: AMBER map at $-277\,\mathrm{km\,s^{-1}}$, where the fan-shaped SE morphology is observed at $\phi \sim 0.91$. *Upper-left panel*: GRAVITY image at $-291\,\mathrm{km\,s^{-1}}$, the SE arc-like feature is observed at $\phi \sim 1.28$. The FOV of the images is of 36 mas, and they are oriented with the east pointing toward the left and the north toward the top of frames. *Lowermost panels*: three orbital phases, $\phi = 0.5$ (*lower-left*), $\phi = 1.0$ (*lower-middle*) and $\phi = 1.1$ (*lower-right*), of the wind-wind collision model created by Madura et al. (2013). The panels show the structure of the wind-wind cavity in the orbital plane. The red lines indicate the contour where the density is $10^{-16}\,\mathrm{g\,cm^{-3}}$ and they highlight the changes in the leading and trailing arms of the wind-wind cavity. The positions of the primary and secondary for each phase are marked on the panels with blue and green dots, respectively. The green, magenta, and yellow areas trace the hot ($T \sim 10^6 - 10^8\,\mathrm{K}$) post-shock secondary wind bordering the cavity shells. The vector of the observer's line-of-sight is labeled on each panel, and it corresponds to $\omega = 243°$ and $\omega = 47°$. The principal components' of the wind-wind cavity are also indicated in the panels. The lowermost panels were taken from Madura et al. (2013) and adapted to the discussion presented in Sect. 4.3.

pressed η_A shells are also dependent on the adopted $\dot{M}_{\eta_A}$. Bordering the compressed shell of primary wind, there is the hot post-shock η_B wind. Due to the increment of orbital speed of η_B as it approaches the periastron, the post-shock η_B wind is heated to higher temperatures ($T \sim 10^6\,\mathrm{K}$) than the gas in the trailing arm ($T \sim 10^4\,\mathrm{K}$), producing an asymmetric hot shock. After the periastron, photo-ablation of the post shock η_A wind could stop the η_B wind from heating the primary wind, enhancing the asymmetric temperature in the inter-cavity between the secondary and (bordering) the compressed shell of primary wind.

In this framework, the 2016 GRAVITY images reveal the structure of the cavity at an orbital phase $\phi \sim 1.3$[5] (upper-left panel in Fig. 12), where the arc-like feature could be interpreted as the inner-most hot post-shock gas flowing along the cavity walls that border the compressed η_A wind shell in our

line-of-sight. The fact that we observe material preferentially along the SE cavity walls, suggests that the half-opening angle is quite similar to the inclination angle of the system.

Madura et al. (2013) shows detailed model snap-shots that illustrate the dependence of the opening angle on the mass-loss rate. However, a straight-forward estimate following the two-wind interaction solution of Canto et al. (1996), keeping constant the secondary mass-loss rate and wind velocities, suggests that a primary mass-loss rate between 5.8×10^{-4} and $1.2 \times 10^{-3}\,M_\odot\,\mathrm{yr^{-1}}$ is necessary to produce a half-opening angle in the cavity of $40°$–$60°$. Smaller mass-loss rates would produce bigger angles, which would prevent the wall of the wind-wind collision cavity from intercepting the LOS. The orientation of the extended emission is also consistent with a prograde motion of the secondary (i.e., $i > 90°$, $\omega > 180°$), with a leading arm projected motion from east to west.

Our analysis of the Brγ arc-like feature's peak in the 2016 images suggests that not all the material is moving at the same speed, Fig. 13 displays the centroid position (flux centroid of the

---

[5] Here, we adopted the 2009 periastron passage, $T_0 = 2454851.7\,\mathrm{JD}$, as reference for the orbital phases labeled on the reconstructed images and diagrams of the wind-wind cavity structure.
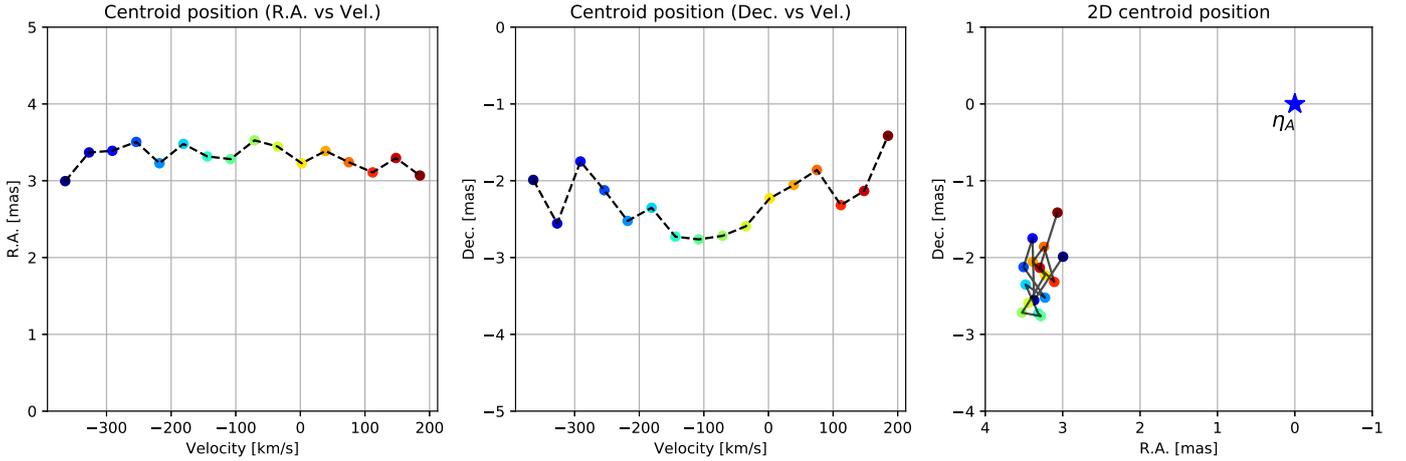
Fig. 13. The image displays the centroid position of the 2016 arc-like feature vs. velocity. *Left panel*: centroid changes in RA vs. velocity. *Middle panel*: centroid changes in Dec vs. velocity. *Right panel*: 2D centroid position relative to the η_A's continuum marked at origin with a blue star.

90% emission peak) of the arc-like feature versus radial velocity. As it is observed, the centroid distribution varies between 3.0 and 4.0 mas (7–9 au) and between −1.5 and −3.0 mas (3.5–7 au) in RA and Dec, respectively. This indicates that the observed material has a clumpy structure that is not expanding at the same speed. It is also consistent with the hydrodynamic simulations which suggest that the stability of the shells depends on the shock thickness and that fragmentation begins later the higher the value of the primary's mass-loss rate.

Furthermore, it also provides a plausible explanation for the structures observed in the 2014 AMBER images (Weigelt et al. 2016), which correspond to a later orbital phase previous to the periastron passage (upper-right panel in Fig. 12), where the shells are disrupted and the hot η_B wind has already mixed with some portions of the compressed η_A wind. In this scenario the bar, observed in the AMBER data between −414 and −352 km s^{-1}, could be part of the highest velocity component of the hot gas around the distorted shell, while the two antennas of the fan-like structure (from −339 to −227 km s^{-1}) could trace portions of the shell that are not yet fragmented. The SE extended emission at lower negative velocities could be interpreted as part of the material bordering the disrupted shell. The observed extended SW emission at positive velocities could be identified as the material flowing along the leading arm's wall which is moving away from the observer at the orbital phase of the AMBER images.

This scenario agrees with observations of the fossil shells on larger spatial scales. Teodoro et al. (2013) observed three progressive shells using HST [Fe II] and [Ni II] spectroimages. Since the emission of the forbidden lines is optically thin, the observed shells in the [Fe II] and [Ni II] images support a future radio mapping with ALMA in H$_\alpha$ lines at an angular resolution better than 0.1″ to properly constrain their emmitting regions. The positions of the arcs are consistent with the SE extended emission observed in the interferometric images, but the HST arcs extend up to 0.5″. Those authors derived a time difference between the arcs of the order of the orbital period (∼5.54 years), suggesting that each one was created during a periastron passage. Assuming a constant shell velocity, Teodoro et al. (2013) derived a traveling speed of the fossil shells of +475 km s^{-1}, with the closest arc to η_A located, in projection, at ∼0.1″ (235 au). Notice that the innermost arc presented in Fig. 2 of Teodoro et al. (2013) resembles the fan-like structure observed in the AMBER images.

It is important to highlight that, while the HST images are tracing the compressed η_A wind in the fossil shells, our Brγ images are tracing the hot gas, bordering them, along the cavity walls. A monitoring of the arc-like features with GRAVITY (using short baselines) will be fundamental to characterize the primary's mass-los rate and the effect of η_B over the primary wind shells over future orbital phases.

4.4. Ionization effect of η_B's wind observed through the He I 2s-2p line

Helium lines are one of the most intriguing spectral features in η Car's spectrum. For example, the discovery of the binary was in part based on spectroscopic variations of the *H*-band He I lines (Damineli 1996; Damineli et al. 1997). Since then, several authors have studied the variations in the helium profiles as a consequence of a binary signature (Groh & Damineli 2004; Nielsen et al. 2007; Humphreys et al. 2008; Damineli et al. 2008b; Mehner et al. 2010, 2012). The different CMFGEN models support that the helium lines could be originated in the densest wind of η_A. Depending on the $\dot{M}$ used, the line-emitting region could be extended from a few au to several hundred au (Hillier et al. 2001, 2006; Groh et al. 2012a, see also Sect. 4.1).

However, these models do not fully reproduce the observed evolution of the He I lines without considering the role of η_B (see e.g., Nielsen et al. 2007; Damineli et al. 2008b). It is still not clear where and how the Helium lines are formed in the wind-wind collision scenario. Humphreys et al. (2008), based on HST observations, suggested that the He I lines originate at spatial scales smaller than 100–200 au (∼40–80 mas), but still the structure of the line-formation region was not indicated. The recent 3D hydrodynamic simulations of Clementel et al. (2015a,b) presented maps of the different ionization regions (He^{0+}, He$^+$, He^{2+}) at the innermost 155 au of η Car's core. These simulations take into account the ionization structure of η_A's wind and the effect of η_B's wind on the collision region for the three different mass-loss rates studied in Madura et al. (2013). These models show that there are several regions composed by He$^+$ that might be responsible for the changes observed in the He I profiles.

The GRAVITY observations presented in this study allowed us to obtain the first milliarcsecond resolution images of the
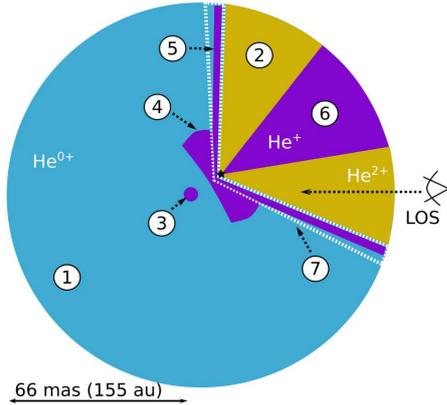
Fig. 14. Different He ionized regions: He^{0+} (blue), He^+ (purple), He^{2+} (yellow). The sketch is oriented in a plane parallel to the line-of-sight and the sky plane. Different regions in the wind-wind collision scenario are labeled. Region 1 represents the He^{0+} zone in the primary wind. Region 2 shows the hot post-shock secondary wind composed by He^{2+}. Regions 3–6 correspond to the zones composed by He^+ in the primary and secondary winds. Region 7 displays the borders of the cavity walls.

inner 20 mas (50 au) He I 2s-2p line-emitting region. In contrast to Brγ, which is observed purely in emission, He I 2s-2p shows a P-Cygni profile with the absorption side blue-shifted. This profile is similar to the helium lines observed at other wavelengths (see e.g., Nielsen et al. 2007). In our images, at velocities between -403 and $-326\,\mathrm{km\,s^{-1}}$, which correspond to the valley of the line, the extended emission is brighter than at other wavelengths. As we move from the valley to the peak of the line, the brightness of the extended emission decreases, slightly increasing again at velocities around the line's peak (between -95 and $-18\,\mathrm{km\,s^{-1}}$). At the red-shifted velocities, the continuum is dominant and the extended component is marginally observed at low-velocities. At the valley of the line, the 2016 images show an elongated emission that is oriented at a PA $\sim 130°$ and it extends on both sides of the continuum, with the southeast side slightly more extended.

To compare the morphological changes observed in the images with the model developed by Clementel et al. (2015a,b), we use an adapted version of the helium distribution presented in Fig. 8 by Clementel et al. (2015b). The schematic diagram, in Fig. 14 displays the distribution of helium, in the inner 155 au of η Car. Region 1 corresponds to the zone in the primary wind that is composed mostly by He^{0+}. Region 2 shows the hot post-shock η_B's wind composed mostly by fully ionized He^{2+}. Regions 3–6 correspond to the zones composed by He^+ and region 7 displays the borders of the cavity walls where compressed post-shock η_A's wind is found.

From the distribution of He^+, four main regions are observed at different morphological scales. The first of them (region 3) corresponds to the pre-shock primary wind that is partially ionized only by η_A. The second zone (region 4) is created by the He^{0+}-ionizing photons from η_B's wind that penetrate the pre-shock primary wind. This region varies in size, being more compact along the azimuthal plane than in the orbital one. Clementel et al. (2015b) argued as possible cause for these differences the less turbulent nature of the wind-wind interaction region in the azimuthal plane. Region 5 shows the He^+, of the post-shock wind of η_A, trapped in the walls of the cavity. Finally, region 6 displays the section of the pre-shock η_B wind with He^+. It is important to highlight that regions 3–5 are expected to be around three orders of magnitude denser than region 6.

The fact that we observe the absorption side of the He I 2s-2p blue-shifted implies that it is formed by material in front of η_A. It means that regions 4–6 are in the LOS. Therefore, the He I 2s-2p structure observed in the GRAVITY images is formed by the different contribution of those regions. By analyzing the images, we hypothesized that the elongated structure, at velocity channels near the valley of the line, appears to be formed by the emission coming mainly from regions 4 and 5. This idea is consistent with the flow of the He^+ pre-shock primary wind, coming toward us at a velocity of $\sim -400\,\mathrm{km\,s^{-1}}$, near the apex of the wind-wind collision zone.

This effect could explain why we observe the most prominent emission at large velocity channels between -403 and $-326\,\mathrm{km\,s^{-1}}$. Given the PA of the observer's LOS and the orbital plane, we expect to observe emission coming from region 4 at the top and bottom of the continuum. This scenario is also consistent with the emission observed in the GRAVITY images. Since the system near apastron is preferentially oriented toward the material in region 4 that borders the lower wall of the cavity, we also expect to observe an asymmetric emission as the one detected in the images.

As we move toward the systemic velocity of the line, we notice that the extended emission decreases in brightness and size, but it increases again at velocity channels near the emission peak. We suspect that this effect is caused by the material in region 5. The post-shock primary wind in the thin walls of the cavity experiences a turbulent environment, particularly at the apex, that causes some of the material to have zero or positive radial velocities. Notice, however, that for velocities larger than $+98\,\mathrm{km\,s^{-1}}$, the main source of the emission is within the size of the primary beam. This suggests that the origin of large red-shifted velocities is the pre-shock ionized wind from η_A (region 3). Hence, similar to Brγ, the observed spatial distribution of He I is in agreement with Clementel et al. (2015a) models with $\dot{M}_{\eta_A}$ close to $10^{-3}M_\odot\,\mathrm{yr^{-1}}$. However, future, new hydrodynamic models of the He I 2s-2p line in addition to a GRAVITY monitoring of the line's morphology are necessary to provide solid constraints on the mass-loss rate of the system.

5. Conclusions

– We present GRAVITY interferometric data of η Car's core. Our observations trace the inner 20 mas (50 au) of the source at a resolution of 2.26 mas. The spectro-interferometric capabilities of GRAVITY allowed us to chromatically image Brγ and He I 2s-2p emission regions with a spectral resolution of $R = 4000$, while the analysis of the Fringe Tracker data allowed us to measure the size of the continuum emission, and the integrated spectrum to characterize the parameters of the primary star.

– From our geometrical model of the Fringe Tracker squared visibilities, we constrained the size of the continuum emission. We derived a mean FWHM angular scale of 2 mas (~ 5 au) and an elongation ratio $\epsilon = 1.06 \pm 0.5$ for the compact continuum emission of η_A, together with an extended over-resolved emission with an angular size of at least 10 mas. These estimates are in agreement with previous interferometric measurements. Some of the plausible hypotheses to explain the observed elongation of the continuum compact emission are the fast rotation of the primary and/or the effect of the wind-wind collision cavity. A future monitoring of the continuum size and elongation with GRAVITY and other interferometric facilities at different wavelengths, in combination with radiative transfer models, would serve to test these scenarios.

– To characterize the properties of η_A's wind, we applied a CMFGEN 1D non-LTE model to the GRAVITY spectrum. Our model reproduces the He I 2s-2p and He I 3p-4s lines, which could not be formed with the parameters used in previous models in the literature. However, the line-emitting regions of the best-fit model are quite small compared to the structure observed in the reconstructed images. These results imply that single-star models are not enough to reproduce all the observational data. Therefore, the role of η_B should be taken into account when modeling the η Car spectrum. Furthermore, when comparing our model with the η Car spectrum in the visible, we could not reproduce the observed metallic features. We suspect that this is caused because many of the metallic lines are forbidden lines with critical electron densities of 10^{7-8} cm^{-3}. With the FEROS aperture, this emission is originating in the fossil wind shells and hence not reproduced in the stellar model.

– Our aperture-synthesis images allowed us to observe the inner wind-wind collision structure of η Car. Previous AMBER interferometric images of Brγ revealed the wind-wind collision cavity produced by the shock of the fast η_B's wind with the slow and dense η_A's wind. Our new 2016 GRAVITY Brγ images show the structure of such cavity at a different orbital phase with a 2.26 mas resolution. The observed morphologies in the images are (qualitatively) in agreement with the theoretical hydrodynamical models of Madura et al. (2013). Particularly interesting is the bright SE arc-like feature, which could be interpreted as the hot post-shock gas flowing along the cavity wall (oriented toward the observer) that border the innermost shell of compressed primary wind, which is formed by the shock of the cavity's trailing arm with the leading arm after the most recent periastron passage.

– Due to the sparseness of the 2017 GRAVITY data the quality of the reconstructed images from this epoch is clearly affected. Therefore, those images could not be used for a direct comparison with the 2016 ones. Nevertheless, our analysis of the interferometric observables, in coincidental baselines, reveals changes in the cavity structure. The ulterior characterization of those changes is subject to future imaging epochs with a less limited $u-v$ coverage than the 2017 data.

– We presented, the first images of the He I 2s-2p line. They were qualitatively interpreted using the model of Clementel et al. (2015a,b). We hypothesized that the observed emission is coming mainly from the He$^+$ at the cavity walls and from a portion of the pre-shock primary wind ionized by the secondary. From the size of the observed emission and the theoretical models, we suspect that the mass-loss rate of the primary is close to 10^{-3} $M_\odot$ yr^{-1}. The emission observed require an active role of η_B to ionize the material near the apex of the wind-wind collision cavity.

– Spectro-interferometric imaging cubes offer us unique information to constrain the wind parameters of η Car, not accessible by other techniques. In this study, we have shown the imaging capabilities of GRAVITY to carry out this task. A future monitoring of η Car over the orbital period (particularly at the periastron passage), in combination with dedicated hydrodynamical models of the imaged K-band lines, will provide a unique opportunity to constrain the stellar and wind parameters of the target, and, ultimately, to predict its evolution and fate.

References

Allard, F., Homeier, D., & Freytag, B. 2012, Phil. Trans. R. Soc. London, Ser. A, 370, 2765

Allen, D. A., & Hillier, D. J. 1993, Proc. Astron. Soc. Aust., 10, 338

Asplund, M., Grevesse, N., Sauval, A. J., Allende Prieto, C., & Blomme, R. 2005, A&A, 431, 693

Baron, F., & Kloppenborg, B. 2010, SPIE Conf. Ser., 7734, 4

Blind, N., Eisenhauer, F., Haug, M., et al. 2014, Proc. SPIE, 9146, 91461U

Brahm, R., Jordán, A., & Espinoza, N. 2017, PASP, 129, 034002

Canto, J., Raga, A. C., & Wilkin, F. P. 1996, ApJ, 469, 729

Clementel, N., Madura, T. I., Kruip, C. J. H., & Paardekooper, J.-P. 2015a, MNRAS, 450, 1388

Clementel, N., Madura, T. I., Kruip, C. J. H., Paardekooper, J.-P., & Gull, T. R. 2015b, MNRAS, 447, 2445

Conti, P. S. 1984, IAU Symp., 105, 233

Conti, P. S., & Niemelä, V. S. 1976, ApJ, 209, L37

Corcoran, M. F. 2005, AJ, 129, 2018

Corcoran, M. F., Hamaguchi, K., Pittard, J. M., et al. 2010, ApJ, 725, 1528

Damineli, A. 1996, ApJ, 460, L49

Damineli, A., Conti, P. S., & Lopes, D. F. 1997, New Astron., 2, 107

Damineli, A., Hillier, D. J., Corcoran, M. F., et al. 2008a, MNRAS, 386, 2330

Damineli, A., Hillier, D. J., Corcoran, M. F., et al. 2008b, MNRAS, 384, 1649

Davidson, K., & Humphreys, R. M. 1997, ARA&A, 35, 1

Davidson, K., Gull, T. R., & Ishibashi, K. 2001, ASP Conf. Ser., 233, 173

Davidson, K., Mehner, A., Humphreys, R. M., Martin, J. C., & Ishibashi, K. 2015, ApJ, 801, L15

Duvert, G., Young, J., & Hummel, C. 2017, A&A, 597, A8

Eisenhauer, F., Perrin, G., Brandner, W., et al. 2008, SPIE Conf. Ser., 7013, 70132A

Eisenhauer, F., Perrin, G., Brandner, W., et al. 2011, The Messenger, 143, 16

Falcke, H., Davidson, K., Hofmann, K.-H., & Weigelt, G. 1996, A&A, 306, L17

Gillessen, S., Eisenhauer, F., Perrin, G., et al. 2010, SPIE Conf. Ser., 7734, 77340Y

Glindemann, A., Algomedo, J., Amestica, R., et al. 2003, SPIE Conf. Ser., 4838, 89

Gomez, H. L., Vlahakis, C., Stretch, C. M., et al. 2010, MNRAS, 401, L48

Gravity Collaboration (Abuter, R., et al.) 2017, A&A, 602, A94

Groh, J. H., & Damineli, A. 2004, IBVS, 5492

Groh, J. H., Madura, T. I., Owocki, S. P., Hillier, D. J., & Weigelt, G. 2010a, ApJ, 716, L223

Groh, J. H., Nielsen, K. E., Damineli, A., et al. 2010b, A&A, 517, A9

Groh, J. H., Hillier, D. J., Madura, T. I., & Weigelt, G. 2012a, MNRAS, 423, 1623

Groh, J. H., Madura, T. I., Hillier, D. J., Kruip, C. J. H., & Weigelt, G. 2012b, ApJ, 759, L2

Gull, T. R., Nielsen, K. E., Corcoran, M. F., et al. 2009, MNRAS, 396, 1308

Gull, T. R., Madura, T. I., Groh, J. H., & Corcoran, M. F. 2011, ApJ, 743, L3

Gull, T. R., Madura, T. I., Teodoro, M., et al. 2016, MNRAS, 462, 3196

Hillier, D. J., & Miller, D. L. 1998, ApJ, 496, 407

Hillier, D. J., Davidson, K., Ishibashi, K., & Gull, T. 2001, ApJ, 553, 837

Hillier, D. J., Gull, T., Nielsen, K., et al. 2006, ApJ, 642, 1098

Hofmann, K.-H., & Weigelt, G. 1988, A&A, 203, L21

Humphreys, R. M., & Davidson, K. 1994, PASP, 106, 1025

Humphreys, R. M., Davidson, K., & Koppelman, M. 2008, AJ, 135, 1249

Kaufer, A., & Pasquini, L. 1998, Proc. SPIE, 3355, 844

Kervella, P., Coudé du Foresto, V., Glindemann, A., & Hofmann, R. 2000, SPIE Conf. Ser., 4006, 31

Kervella, P., Schöller, M., van Boekel, R., et al. 2002, ASP Conf. Ser., 279, 99

Langer, N. 1998, A&A, 329, 551

Langer, N., Hamann, W.-R., Lennon, M., et al. 1994, A&A, 290, 819

Lapeyrere, V., Kervella, P., Lacour, S., et al. 2014, SPIE Conf. Ser., 9146, 91462D

Madura, T. I., & Groh, J. H. 2012, ApJ, 647, L18

Madura, T. I., Gull, T. R., Owocki, S. P., et al. 2012, MNRAS, 420, 2064

Madura, T. I., Gull, T. R., Okazaki, A. T., et al. 2013, MNRAS, 436, 3820

Mehner, A., Davidson, K., Ferland, G. J., & Humphreys, R. M. 2010, ApJ, 710, 729

Mehner, A., Davidson, K., Humphreys, R. M., et al. 2012, ApJ, 751, 73

Mehner, A., Ishibashi, K., Whitelock, P., et al. 2014, A&A, 564, A14

Meynet, G., & Maeder, A. 2003, A&A, 404, 975

Meynet, G., Georgy, C., Hirschi, R., et al. 2011, Bull. Soc. Roy. Sci. Liège, 80, 266

Millour, F., Vannier, M., Petrov, R. G., et al. 2006, EAS Pub. Ser., 22, 379

Millour, F., Petrov, R. G., Chesneau, O., et al. 2007, A&A, 464, 107

Morris, P. W., Gull, T. R., Hillier, D. J., et al. 2017, ApJ, 842, 79

Nielsen, K. E., Ivarsson, S., & Gull, T. R. 2007, ApJS, 168, 289

Okazaki, A. T., Owocki, S. P., Russell, C. M. P., & Corcoran, M. F. 2008, MNRAS, 388, L39

Parkin, E. R., Pittard, J. M., Corcoran, M. F., Hamaguchi, K., & Stevens, I. R. 2009, MNRAS, 394, 1758

Parkin, E. R., Pittard, J. M., Corcoran, M. F., & Hamaguchi, K. 2011, ApJ, 726, 105

Pastorello, A., Botticella, M. T., Trundle, C., et al. 2010, MNRAS, 408, 181

Patil, A., Huard, D., & Fonnesbeck, C. J. 2010, J. Stat. Softw., 35, 1

Pauls, T. A., Young, J. S., Cotton, W. D., & Monnier, J. D. 2005, PASP, 117, 1255

Petrov, R. G., Malbet, F., Weigelt, G., et al. 2007, A&A, 464, 1

Pittard, J. M., & Corcoran, M. F. 2002, A&A, 383, 636

Richardson, N. D., Gies, D. R., Gull, T. R., Moffat, A. F. J., & St-Jean, L. 2015, AJ, 150, 109

Richardson, N. D., Madura, T. I., St-Jean, L., et al. 2016, MNRAS, 461, 2540

Sanchez-Bermudez, J., Alberdi, A., Barbá, R., et al. 2017, ApJ, 845, 57

Smith, N. 2006, MNRAS, 367, 763

Smith, N. 2007, AIP Conf. Ser., 937, 163

Smith, N., Bally, J., & Morse, J. A. 2003, ApJ, 587, L105

Smith, N., Gehrz, R. D., Campbell, R., et al. 2011, MNRAS, 418, 1959

Steffen, W., Teodoro, M., Madura, T. I., et al. 2014, MNRAS, 442, 3316

Teodoro, M., Damineli, A., Sharp, R. G., Groh, J. H., & Barbosa, C. L. 2008, MNRAS, 387, 564

Teodoro, M., Madura, T. I., Gull, T. R., Corcoran, M. F., & Hamaguchi, K. 2013, ApJ, 773, L16

Teodoro, M., Damineli, A., Heathcote, B., et al. 2016, ApJ, 819, 131

Trundle, C., Kotak, R., Vink, J. S., & Meikle, W. P. S. 2008, A&A, 483, L47

van Boekel, R., Kervella, P., Schöller, M., et al. 2003, A&A, 410, L37

Walborn, N. R. 1973, ApJ, 179, 517

Weigelt, G., & Ebersberger, J. 1986, A&A, 163, L5

Weigelt, G., Albrecht, R., Barbieri, C., et al. 1995, Rev. Mex. Astron. Astrofis., 2, 11

Weigelt, G., Kraus, S., Driebe, T., et al. 2007, A&A, 464, 87

Weigelt, G., Hofmann, K.-H., Schertl, D., et al. 2016, A&A, 594, A106

[1] Max Planck Institute for Astronomy, Königstuhl 17, 69117 Heidelberg, Germany
e-mail: sanchezj@eso.org

[2] LESIA, Observatoire de Paris, PSL Research University, CNRS, Sorbonne Universités, UPMC Univ. Paris 06, Univ. Paris Diderot, Sorbonne Paris Cité, France

[3] Univ. Grenoble Alpes, CNRS, IPAG, 38000 Grenoble, France

[4] I. Physikalisches Institut, Universität zu Köln, Zülpicher Str. 77, 50937 Köln, Germany

[5] Universidade do Porto – Faculdade de Engenharia, Rua Dr. Roberto Frias, 4200-465 Porto, Portugal

[6] CENTRA, Instituto Superior Tecnico, Av. Rovisco Pais, 1049-001 Lisboa, Portugal

[7] European Southern Observatory, Karl-Schwarzschild-Str. 2, 85748 Garching, Germany

[8] European Southern Observatory, Casilla 19001 Santiago 19, Chile

[9] Max Planck Institute for Extraterrestrial Physics, Giessenbachstrasse, 85741 Garching bei München, Germany

[10] Dublin Institute for Advanced Studies, 31 Fitzwilliam Place, D02 XF86 Dublin, Ireland

[11] Max-Planck-Institute for Radio Astronomy, Auf dem Hügel 69, 53121 Bonn, Germany

[12] Department of Physics, Le Conte Hall, University of California, Berkeley, CA 94720, USA

[13] Unidad Mixta Internacional Franco-Chilena de Astronomía (CNRS UMI 3386), Departamento de Astronomía, Universidad de Chile, Camino El Observatorio 1515, Las Condes, Santiago, Chile

[14] Sterrewacht Leiden, Leiden University, Postbus 9513, 2300 RA Leiden, The Netherlands

[15] Department of Physics and Astronomy, University of Sheffield, Hicks Building, Hounsfield Rd., Sheffield S3 7RH, UK

[16] Observatoire de Genève, Université de Genève, 51 Ch. des Maillettes, 1290 Sauverny, Switzerland

[17] ONERA, The French Aerospace Lab, Châtillon, France

[18] European Space Agency, Space Telescope Science Institute, Baltimore, USA

[19] Faculdade de Ciências, Universidade de Lisboa, Edifício C8, Campo Grande, 1749-016 Lisbon, Portugal

[20] School of Physics, Astrophysics Group, University of Exeter, Stocker Road, Exeter EX4 4QL, UK

Appendix A: GRAVITY observations' lists

Table A.1. η Car's 2016 GRAVITY observations.

Date	Source	MJD	Type	DIT	NDIT	Airmass	Seeing
24-02-2016	η Car	57443.0859	SCI	10	30	1.479	0.83
	η Car	57443.0951	SCI	10	30	1.440	0.89
	HD 89 682	57443.1119	CAL	10	30	1.267	0.82
	η Car	57443.1342	SCI	10	30	1.315	1.09
	η Car	57443.1427	SCI	10	30	1.295	0.85
	HD 89 682	57443.1646	CAL	10	30	1.175	0.87
	HD 89 682	57443.1780	CAL	10	30	1.165	0.99
	HD 89 682	57443.1890	CAL	10	30	1.161	0.95
	η Car	57443.2026	SCI	10	30	1.224	0.78
	η Car	57443.2142	SCI	10	30	1.222	1.05
	HD 89 682	57443.2315	CAL	10	30	1.331	1.03
	η Car	57443.2689	SCI	10	30	1.263	0.77
	η Car	57443.2855	SCI	10	30	1.293	0.98
	HD 89 682	57443.3078	CAL	10	30	1.350	1.16
	HD 89 682	57443.3692	CAL	10	30	1.706	–
	η Car	57443.3878	SCI	10	30	1.746	–
	η Car	57443.3962	SCI	10	30	1.814	–
	HD 89 682	57443.4103	CAL	10	30	2.170	–
27-02-2016	HD 89 682	57446.2508	CAL	10	30	1.367	1.38
	HD 89 682	57446.2576	CAL	10	30	1.379	1.03
	η Car	57446.2740	SCI	10	30	1.286	1.01
	η Car	57446.2822	SCI	10	30	1.303	0.90
	η Car	57446.2911	SCI	10	30	1.325	1.06
	η Car	57446.2995	SCI	10	30	1.348	0.94

Table A.2. η Car's 2017 GRAVITY observations.

Date	Source	MJD	Type	DIT	NDIT	Airmass	Seeing
30-05-2017	HD 89 682	57903.9623	CAL	10	30	1.170	0.77
	HD 89 682	57903.9704	CAL	10	30	1.177	1.08
	η Car	57903.9823	SCI	10	30	1.234	0.85
	η Car	57903.9905	SCI	10	30	1.241	0.80
	η Car	57903.9945	SCI	10	30	1.246	0.79
01-06-2017	η Car	57906.0526	SCI	10	30	1.385	0.55
	η Car	57906.0607	SCI	10	30	1.413	0.56
	η Car	57906.0647	SCI	10	30	1.429	0.46
	η Car	57906.0728	SCI	10	30	1.462	0.61
	η Car	57906.0772	SCI	10	30	1.482	0.55
	η Car	57906.0854	SCI	10	30	1.521	0.68
	η Car	57906.0894	SCI	10	30	1.542	0.58
	HD 89 682	57906.1007	CAL	10	30	1.693	0.56

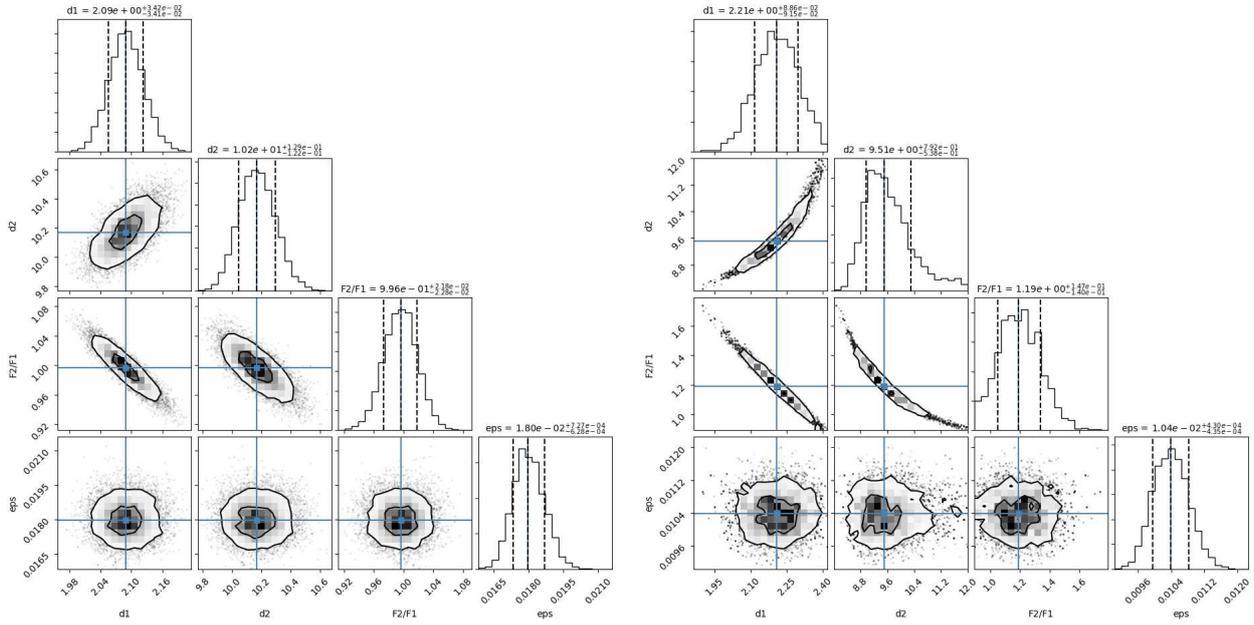## Appendix B: Posterior distributions of the best-fit geometrical model

Fig. B.1. Posterior distributions of the best-fit parameters of the geometrical model presented in Sect. 3.1. *Left panel*: posterior distributions for the model applied to the V^2 data at $PA_\perp = 40° \pm 20°$, while the *right panel* displays the posterior distributions for the model at $PA_\parallel = 130° \pm 20°$. The 2D distributions show 1 and 2 standard deviations encircled with a black contour. The mean of each distribution is displayed with a blue square. The 1D histograms show the expected value (mean) and $\pm 1\sigma$ with vertical dashed lines, together with their corresponding values at the top.

Appendix C: Dirty beams of the GRAVITY imaging epochs
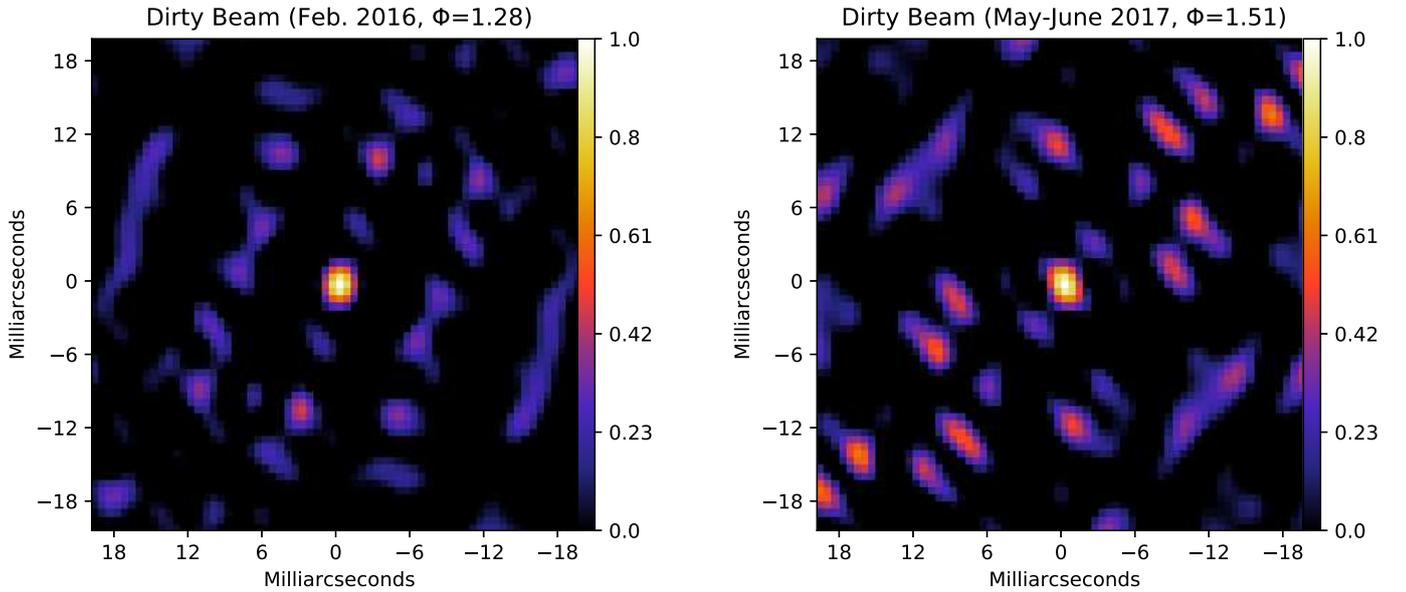
Fig. C.1. Dirty beams of the 2016 (*left*) and 2017 (*right*) GRAVITY data. Notice the strong secondary lobes caused by the more sparse $u-v$ coverage of the second epoch.

Appendix D: Reconstructed Brγ and He I images from the 2017 GRAVITY data
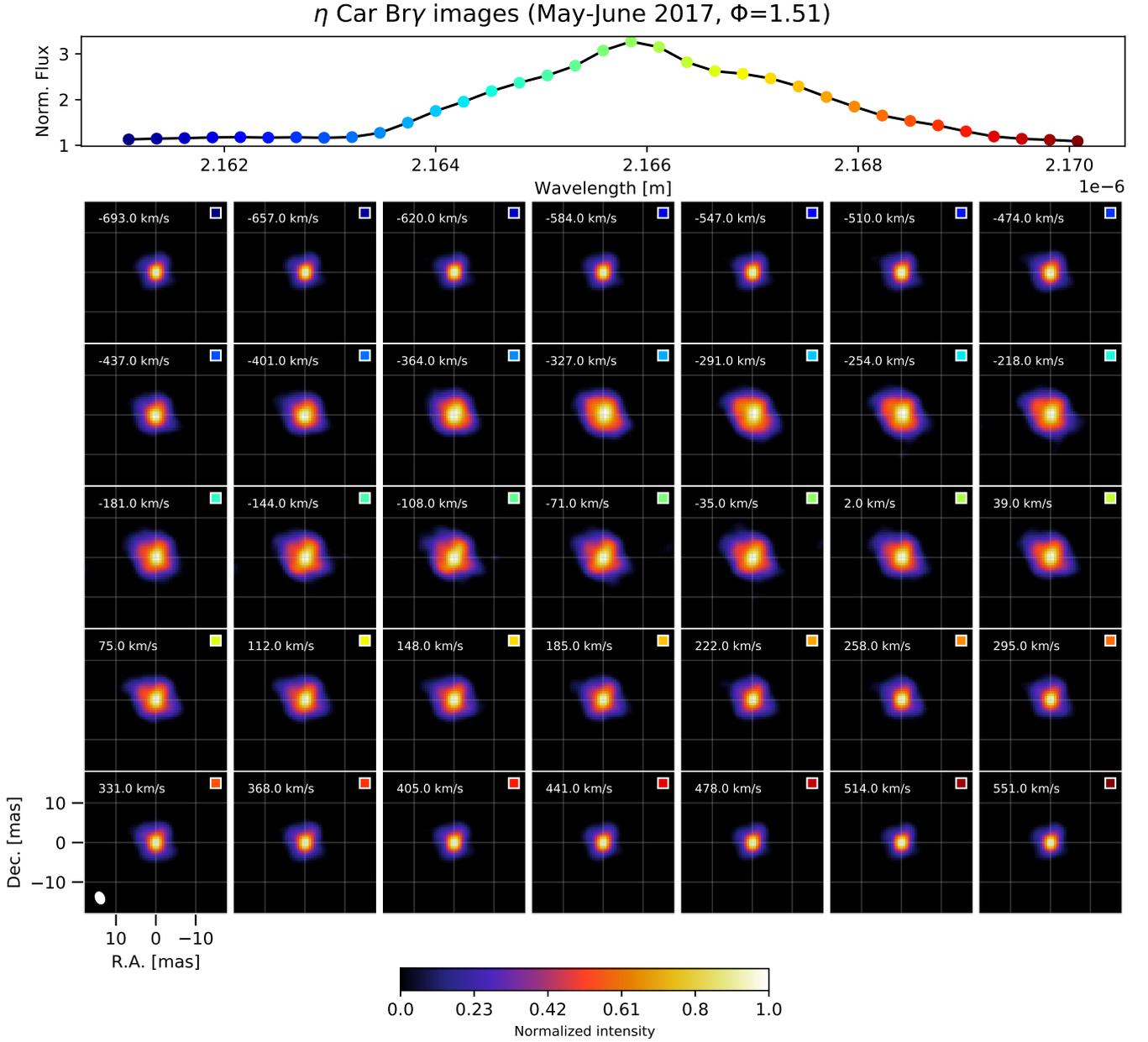
Fig. D.1. Brγ interferometric aperture synthesis images from the May–June 2017 data. The Doppler velocity of each frame is labeled in the images. For all the panels, east is to the left and north to the top and the displayed FOV corresponds to 36 × 36 mas. The small white ellipse shown in the *lowermost-left panel* corresponds to the synthesized beam (the detailed PSF is shown in Fig. D.1). Above all the images, the GRAVITY spectrum is shown and the different positions where the images are reconstructed across the line are labeled with a colored square, which is also plotted in the images for an easy identification. Due to the sparseness of the $u-v$ coverage, the quality of these reconstructed images is limited, creating a clumpy fine structure and a cross-like shape superimposed on the source's brightness distribution. Therefore, they cannot be properly compared with the GRAVITY 2016 data presented in this work.

η Car HeI images (May-June 2017, Φ=1.51)
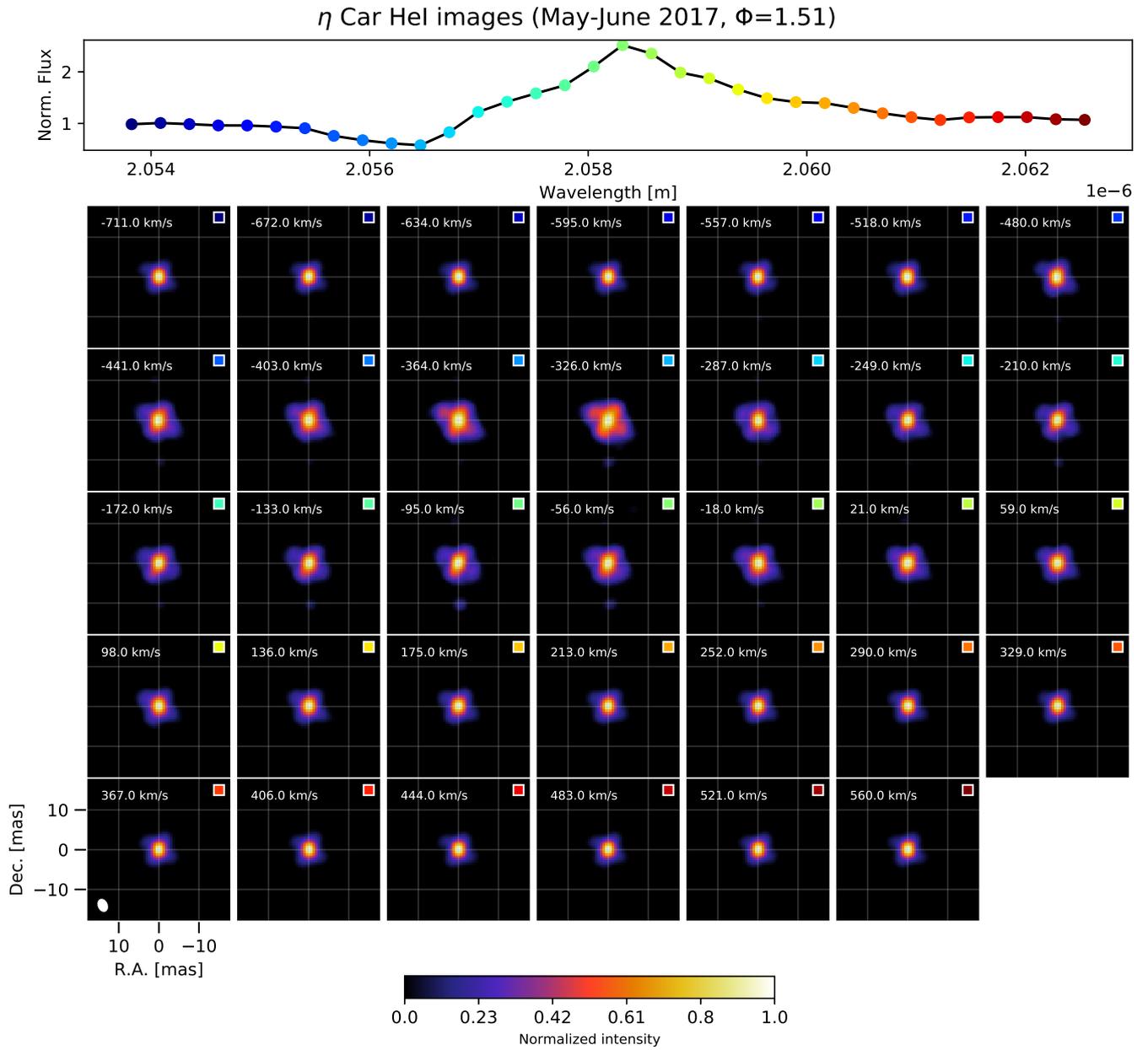
Fig. D.2. He I interferometric aperture synthesis images from the May–June 2017 data. The maps are as described in Fig. D.1.

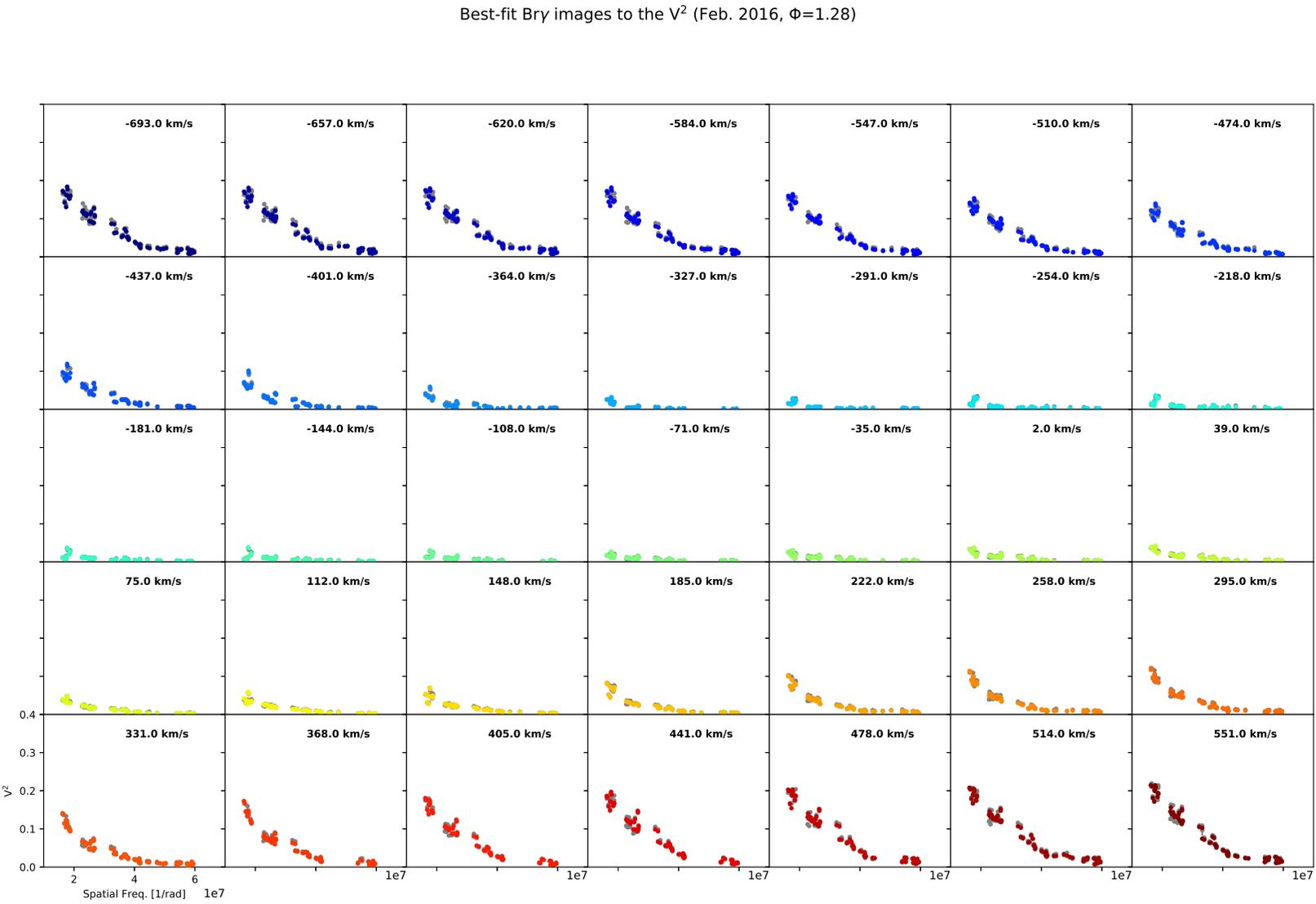**Appendix E: Best-fit of the reconstructed images to the V² and closure phases**

Best-fit Brγ images to the V² (Feb. 2016, Φ=1.28)

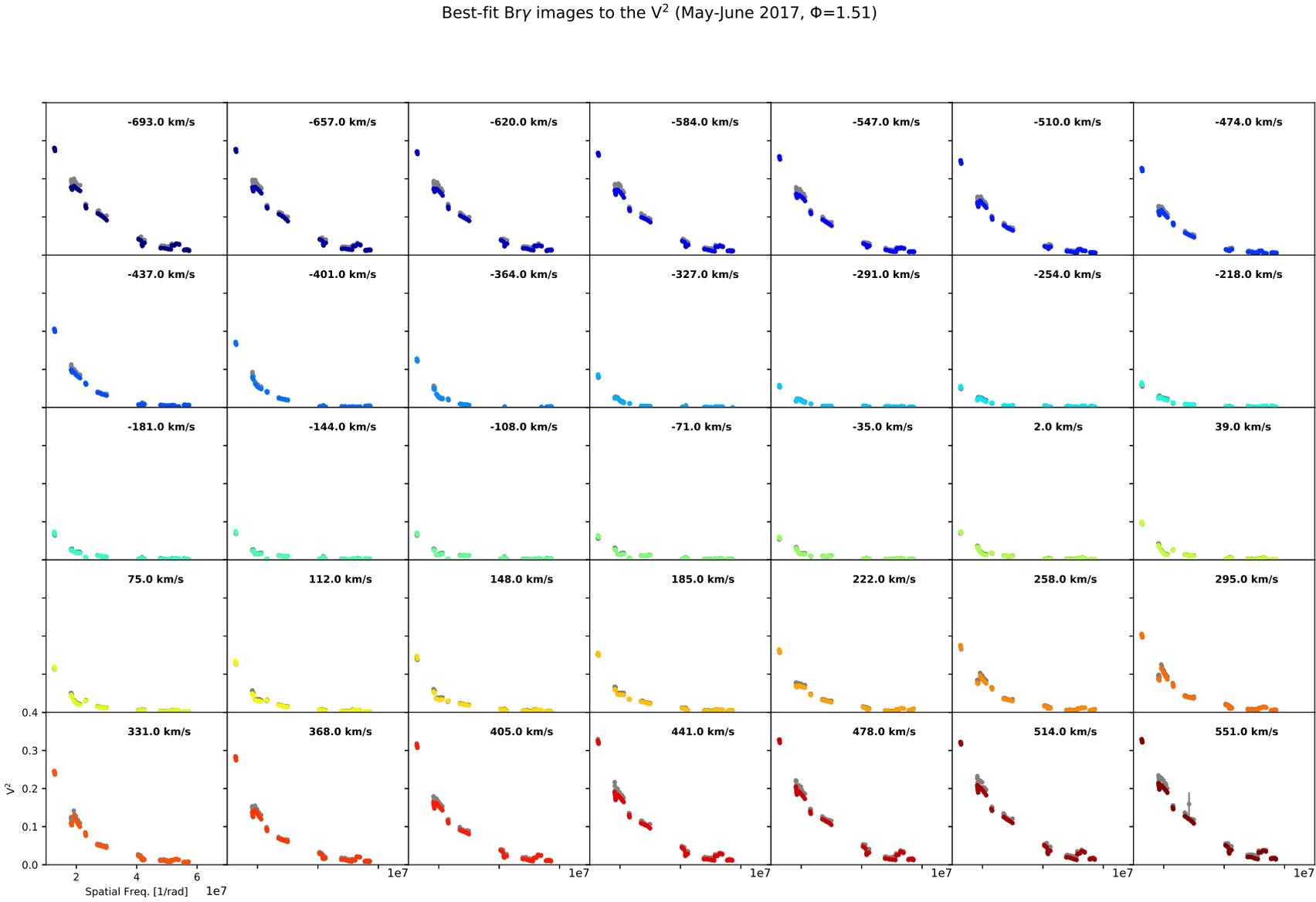**Fig. E.1.** Fit to the observed V^2 from the interferometric aperture synthesis images across the Brγ line (2016). The colored dots correspond to the synthetic V^2 extracted from the unconvolved reconstructed images, while the observational data are represented with gray dots with 1σ error-bars. The Doppler velocity is labeled in each panel. All the panels share the same horizontal and vertical scales.
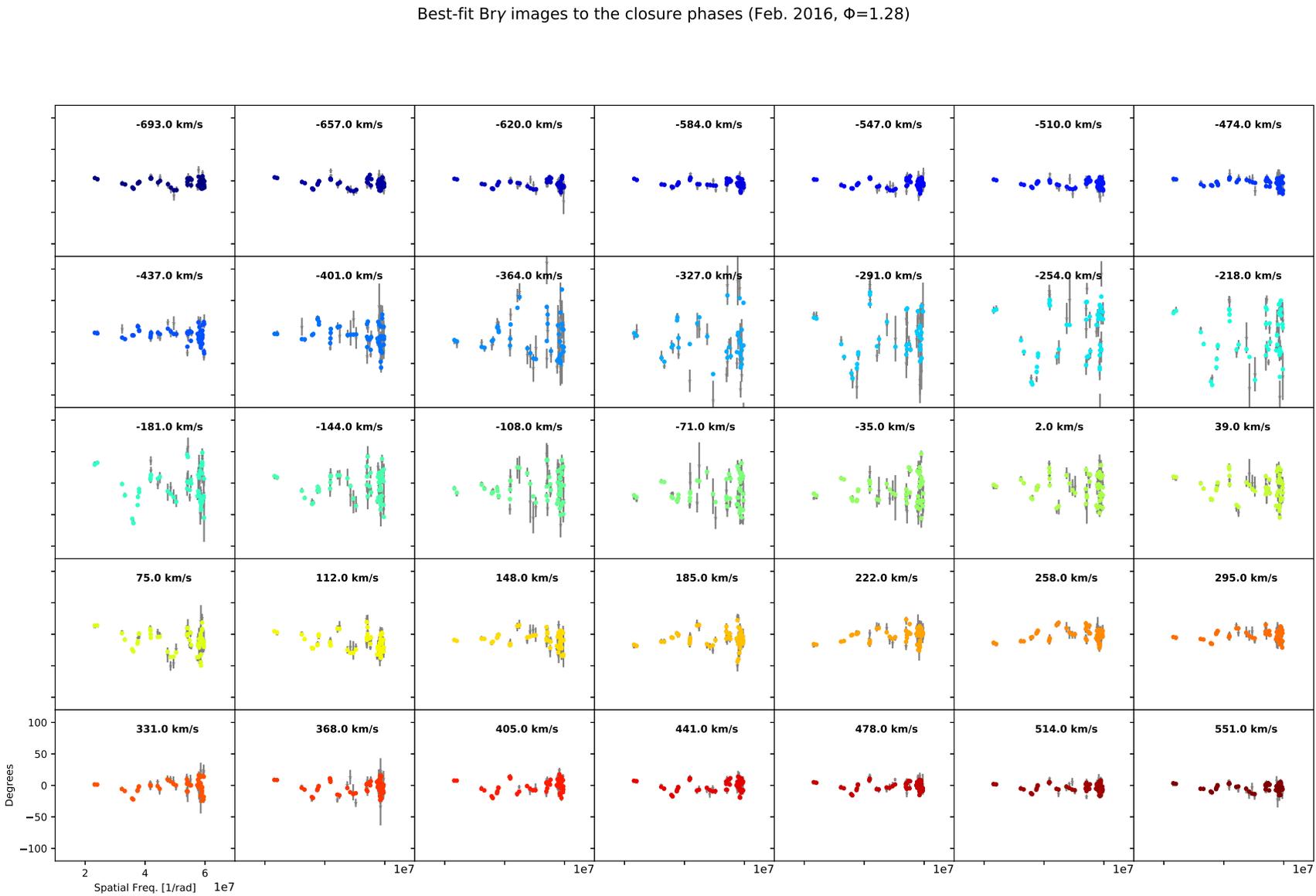
Fig. E.2. Fit to the observed closure phases from the interferometric aperture synthesis images across the Brγ line (2016). The panels are as described in Fig. E.1.

Best-fit Brγ images to the closure phases (Feb. 2016, Φ=1.28)

Fig. E.3. Fit to the observed V^2 from the interferometric aperture synthesis images across the Brγ line (2017). The panels are as described in Fig. E.1.
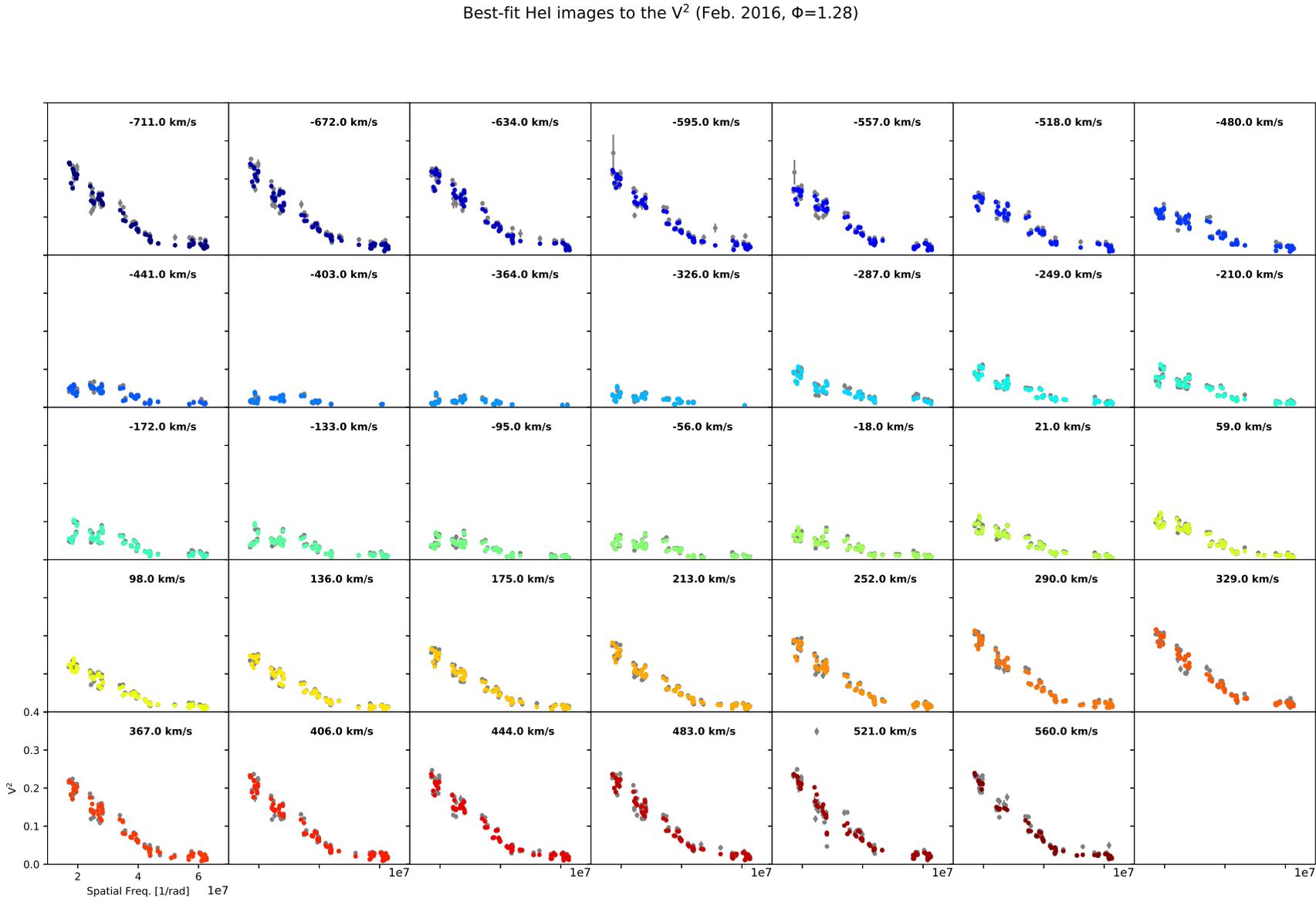
Best-fit Brγ images to the V^2 (May-June 2017, Φ=1.51)

V^2

Spatial Freq. [1/rad]

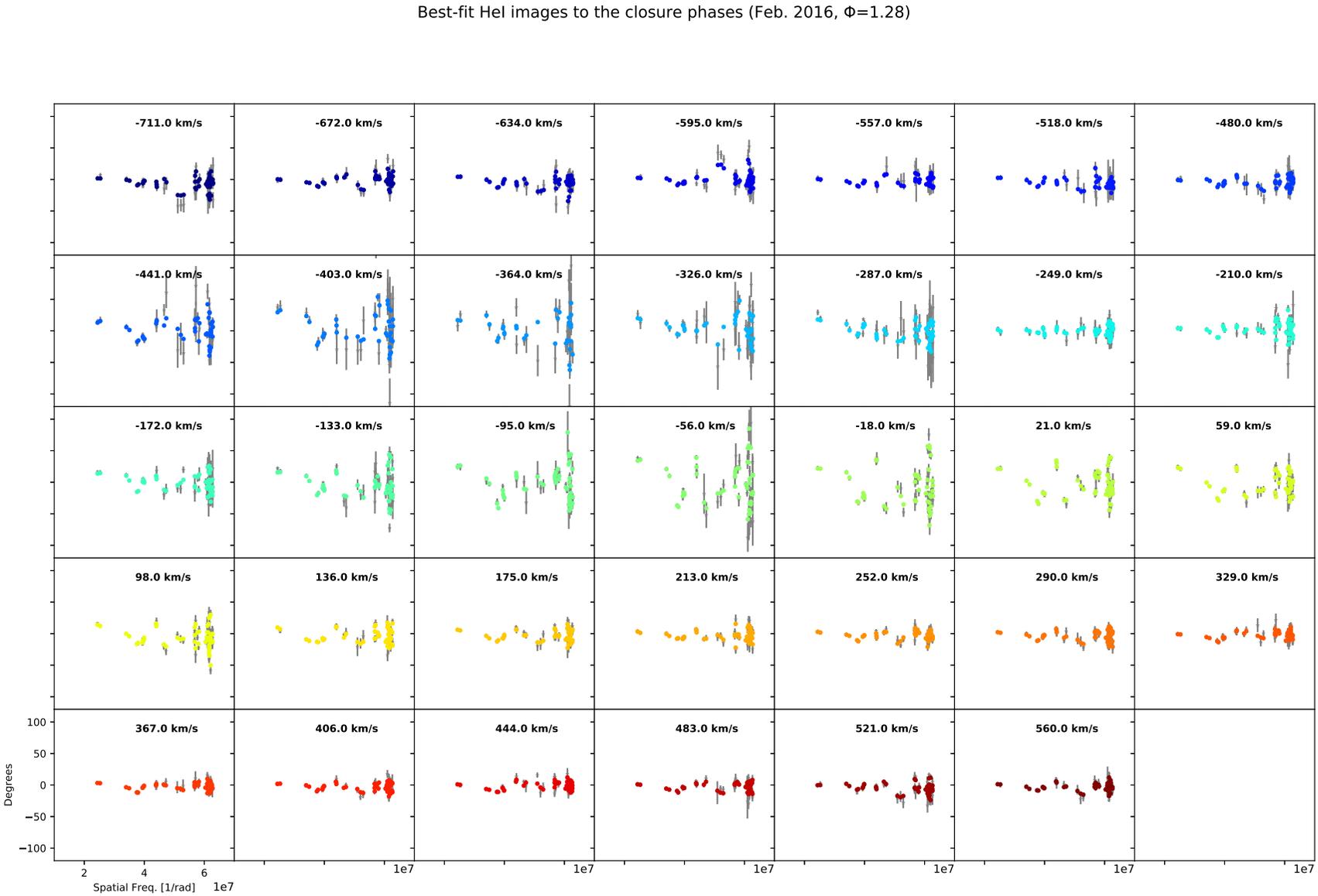Best-fit Brγ images to the closure phases (May-June 2017, Φ=1.51)

Fig. E.4. Fit to the observed closure phases from the interferometric aperture synthesis images across the Brγ line (2017). The panels are as described in Fig. E.1.
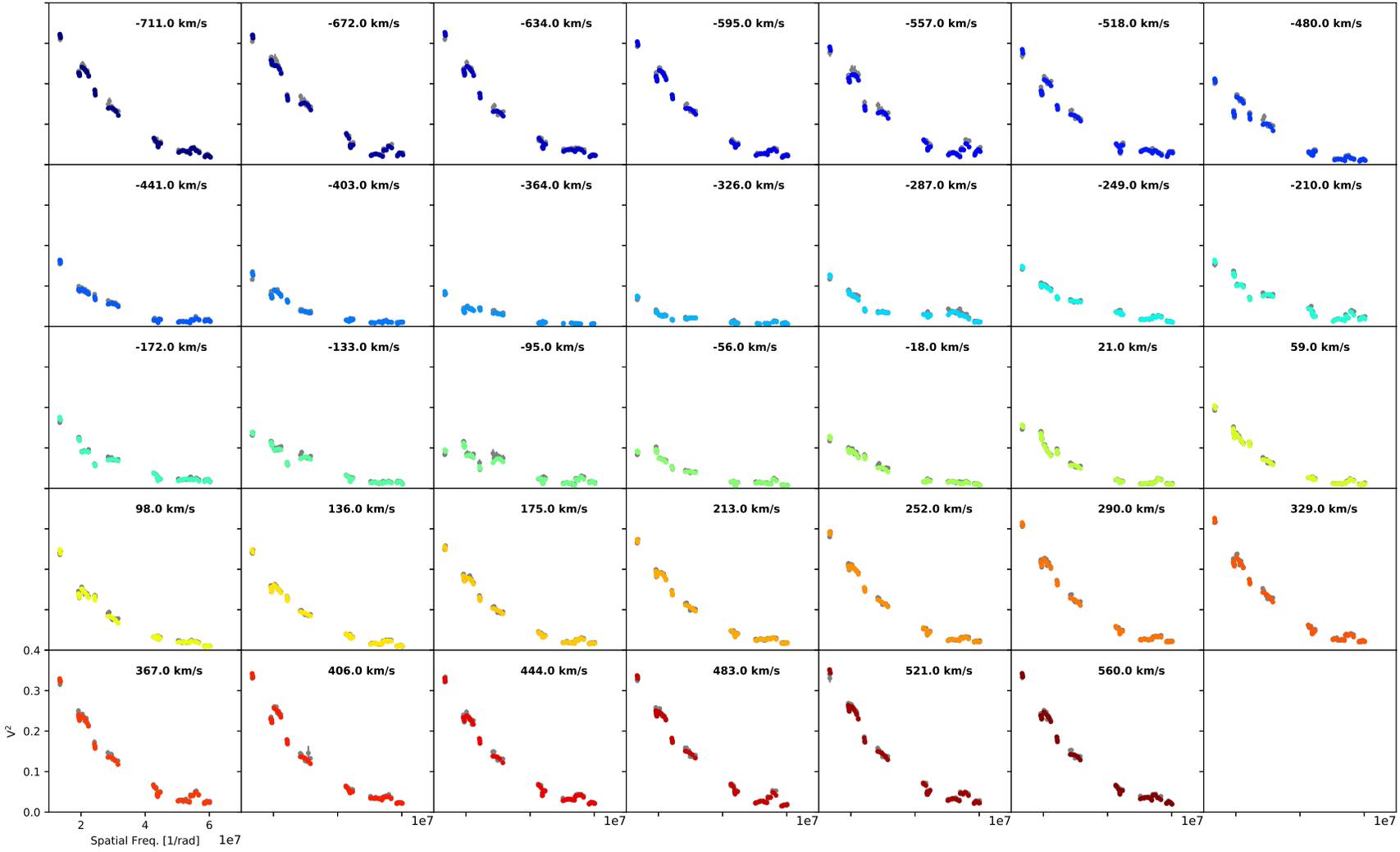
Best-fit HeI images to the V² (Feb. 2016, Φ=1.28)

Fig. E.5. Fit to the observed V² from the interferometric aperture synthesis images across the He I line (2016). The panels are as described in Fig. E.1.

Best-fit HeI images to the closure phases (Feb. 2016, Φ=1.28)
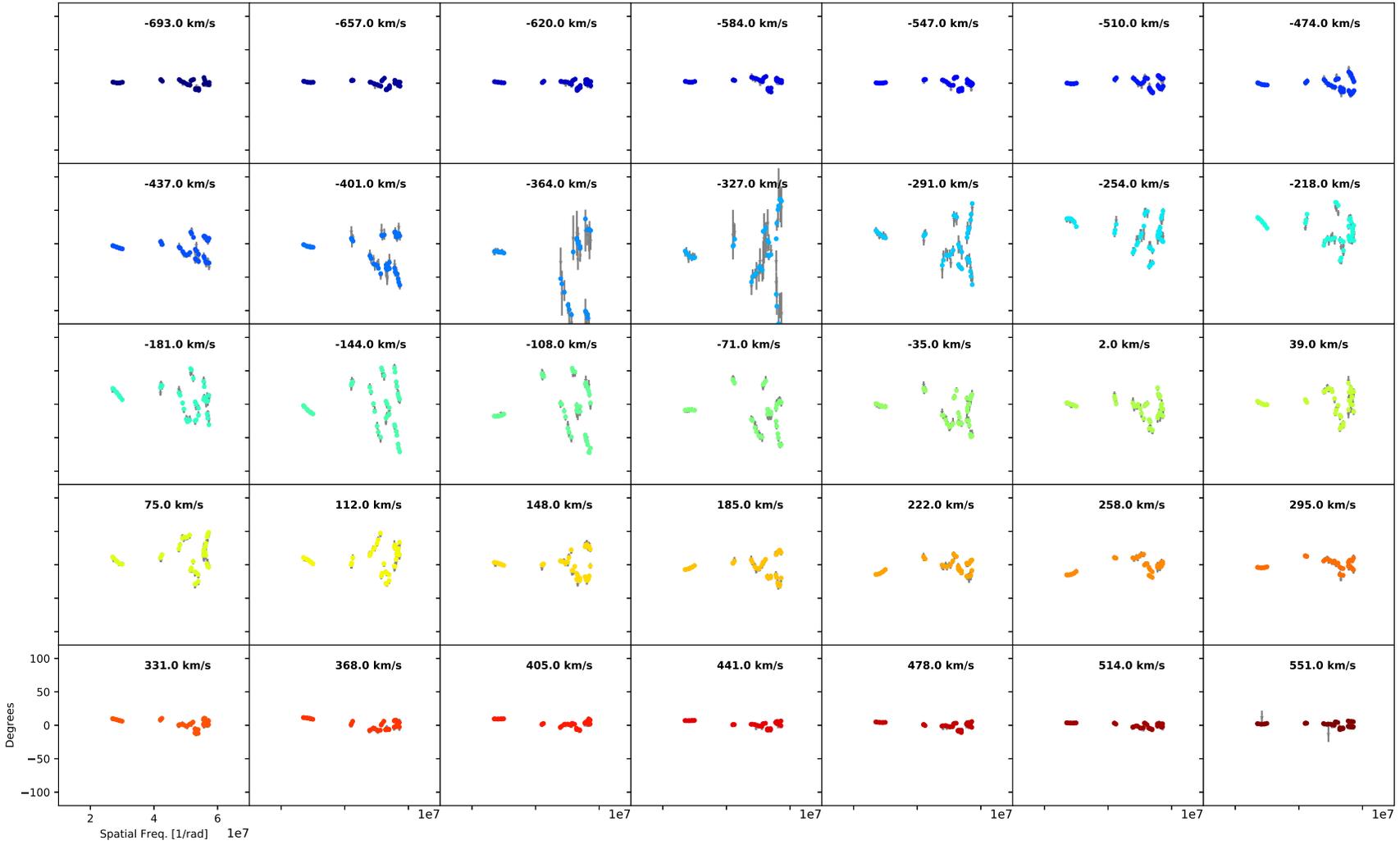
Fig. E.6. Fit to the observed closure phases from the interferometric aperture synthesis images across the He I line (2016). The panels are as described in Fig. E.1.

Best-fit HeI images to the V² (May-June 2017, Φ=1.51)

Fig. E.7. Fit to the observed V² from the interferometric aperture synthesis images across the He I line (2017). The panels are as described in Fig. E.1.
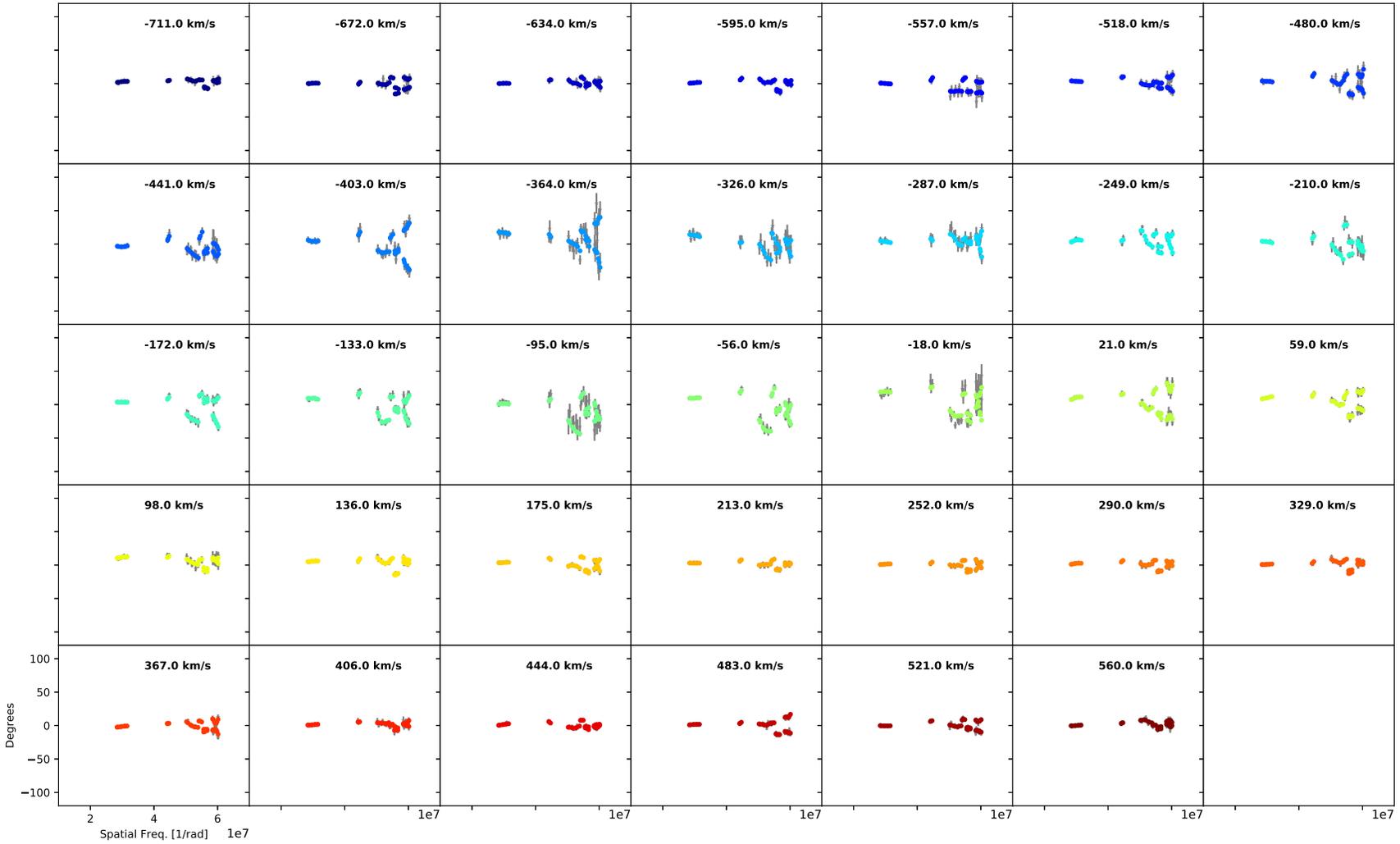
Best-fit HeI images to the closure phases (May-June 2017, Φ=1.51)

Fig. E.8. Fit to the observed closure phases from the interferometric aperture synthesis images across the He I line (2017). The panels are as described in Fig. E.1.
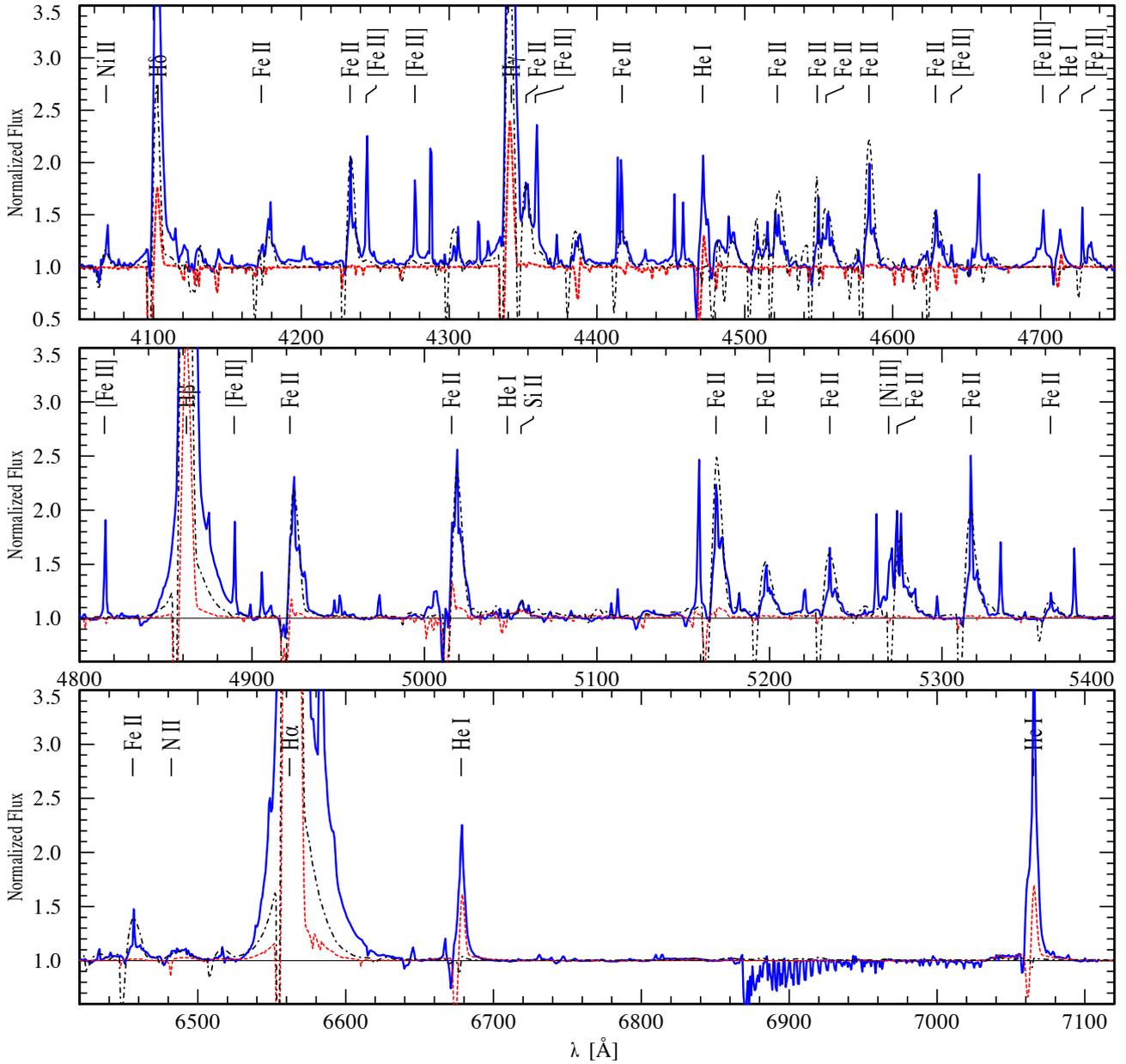
Appendix F: `CMFGEN` models of the FEROS η Car spectrum

Fig. F.1. 2016 η Car's FEROS spectrum (blue-solid line). The image displays our best-fit `CMFGEN` model (red-dashed line) and the model described in Groh et al. (2012a; black-dashed line). The Balmer lines of the FEROS spectrum are too strong. They include large contributions of the circumstellar emission as a result of the bad seeing of ~2″ at the time of the observation. The black synthetic spectrum matches the Fe II and Si II lines. The absorption component of the P-Cygni profiles are filled in and the He I emission lines are not reproduced by the model, which has been already observed and discussed in detail by Hillier et al. (2001). The hotter red model can hardly fit the spectral lines observed at FEROS' wavelengths.